

Electrical characterization of strained $\text{InP-Ga}_x\text{In}_{1-x}\text{As}$ core-shell nanowires

Lorenz Frevel

Thesis submitted for the degree of Master of Physics

Project duration: 8 months

Supervised by Magnus Borgström



LUND
UNIVERSITY

Department of Physics
Division of Solid State Physics
May 2016

Abstract

This project report attempts to measure the piezoelectric effect in strained core-shell nanowires. The core material is wurtzite indium phosphide (InP) and the shell material wurtzite gallium indium arsenide ($\text{Ga}_x\text{In}_{1-x}\text{As}$). The lattice constant of $\text{Ga}_x\text{In}_{1-x}\text{As}$ can be adjusted by its composition x and enables positive and negative strain for core and shell. A piezoelectric fields in the order of $1 \times 10^6 \text{ V m}^{-1}$ was predicted using analytical calculations of the strain. The nanowire samples are grown using metal-organic vapor phase epitaxy (MOVPE), resulting in nanowires with varying shell thickness and shell composition. Single nanowires were contacted to measure their current voltage characteristics. The extracted resistance and rectification behaviour was dominated by the shell thickness for the case of thin shells ($<10 \text{ nm}$). The characteristics of a piezoelectric field, however, could not be extracted from the measurement results.

Acknowledgements

I want to thank my supervisor Magnus Borgström for offering me the opportunity to realize my project in his group with all the required support. I shared the project with David Göransson, who spent a lot of time and effort to introduce me to the practical work in the laboratory and the theory behind the experiments. I am grateful for the gripping discussions and the encouragement. Moreover, I want to thank my loving girlfriend and family for the caring support.

Contents

1	INTRODUCTION	3
2	STRAINED HETEROSTRUCTURES	7
2.1	Qualitative model of strained heterostructures	7
2.2	Quantitative model of strained heterostructures	9
3	GROWTH	14
3.1	Metal Organic Vapor Phase Deposition	15
3.2	Gold seeded growth	16
3.3	Selective area epitaxy	20
4	ELECTRICAL MEASUREMENTS	25
4.1	Experimental details	25
4.1.1	Device fabrication	25
4.1.2	Electrical measurements on individual nanowires	27
4.1.3	Morphology of individual nanowires	29
4.2	Results and Discussion	30
4.2.1	Gold seeded $\text{Ga}_x\text{In}_{1-x}\text{As-InP}$ core-shell nanowires	30
4.2.2	SAE InAs-InP core-shell nanowires	35
4.3	Conclusion	37
5	OUTLOOK	39
A	STRAIN CALCULUS	45

Chapter 1

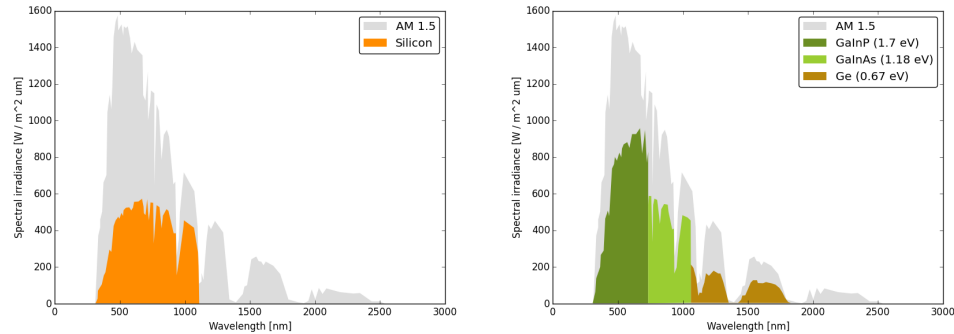
INTRODUCTION

A growing world population with the goal of increasing average wealth cannot base its growth solely on consumption of limited natural resources. In the last decade, renewable energies have shown their potential to contribute to a cleaner energy production. Particularly the use of solar radiation offers great possibilities. It provides about 5000 times more energy than the current world consumption per year [1]. Harvesting only a small portion of that energy could therefore drastically reduce the emissions of energy production and the connected climate change. For that reason the development of photovoltaic cells has become a large research field.

Nowadays commercial wafer based silicon modules are dominating the market due to their decent efficiency of about 16%, relatively low costs, and high reliability. Highly efficient modules could only be competitive in combination with large collectors. That solution provides high efficiencies at reduced costs per module-area. In order to improve the efficiency in a photovoltaic module, mainly the bandgap of the semiconductor material, which determines the distribution of absorbed wavelengths, is modified. A promising material system for that purpose is the use of III-V semiconductors. Various element combinations in binary, ternary or higher order systems provide a high flexibility to adjust the bandgap and ergo the spectral range of absorption. Their predominantly direct bandgap contributes to high absorption coefficients [2]. Figures 1.1a and 1.1b illustrate the difference between silicon based and III-V multijunction solar cells. In the latter case, higher conversion efficiencies and manipulation of the absorption range help to avoid thermalization losses.

Usually III-V semiconductor solar cells are fabricated in thin layers via

Figure 1.1: The AM1.5 solar spectrum with theoretical absorption of different solar cells.



(a) AM 1.5 solar spectrum and theoretical absorption of silicon solar cells after thermalization and transmission losses.

(b) AM 1.5 solar spectrum and theoretical absorption of $\text{Ga}_{0.35}\text{In}_{0.65}\text{P}$ / $\text{Ga}_{0.83}\text{In}_{0.17}\text{As}$ / Ge solar cells with reduced thermalization losses.

metal-organic vapor phase epitaxy (MOVPE). However, thin layers exhibit high surface recombinations of photogenerated carriers and long collection lengths for excited carriers. In contrast, nanowires with a high length-to-diameter ratio provide short collection lengths perpendicular to the main axis of the wire and high electron mobilities. Nanowires (NWs) also can have high crystal qualities and accommodate an increasing amount of strain with decreasing diameter [1]. The latter provides higher flexibility for material combinations directly grown on each other. Jesper Wallentin et al. [3] demonstrated in 2013 that an array of Indium Phosphide (InP) NWs yielded efficiencies of 13.8%. The device generated 83% of the bulk-photocurrent, covering only 12% of the surface. This means that a fraction of material can yield photocurrents close to bulk materials. The drawbacks of those nanowire structures are the difficulties in fabrication, especially the doping of the structures. Replacing the effect of doping would simplify the process to a large extent.

This is the starting point for my project in the group of Magnus Borgström at the department of Solid State Physics in Lund. The idea is that electron hole pairs, which can be created by a photon, are separated by a piezopotential (see figure 1.2) in strained heterostructures. In conventional semiconductor solar cells, they are created by the potential of the depletion region in p-n or p-i-n junctions. The question of whether this field is strong enough to

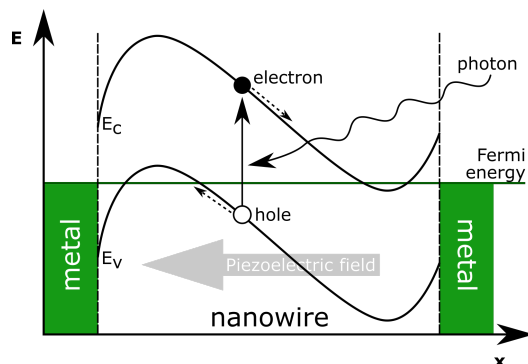


Figure 1.2: Schematic drawing of electron hole separation by a piezoelectric field in a contacted nanowire.

separate electron hole pairs was answered by Frederik Boxberg in 2010 [4]. The group used an analytical model and numerical simulations to investigate strain in nanowires with an Indium Arsenide (InAs) core and an InP shell. They found that the piezoelectric field can exceed 1 V m^{-1} and concluded that the potential created by the piezoelectric field is indeed strong enough to cause charge separation of photogenerated electron hole pairs. Another theoretical work on the piezoelectric field comes from the group around Hanan Al-Zahrani [5]. They simulated the deflection of various III-V semiconductor core shell nanowires by an AFM tip and calculated the polarization of the systems. They concluded that the piezoelectric constants could be higher than previously assumed and that a strong dipole is created along the main axis of the wire. XiaoLong Feng [6] studied the piezotronic heterojunction in axial heterostructures.

In spite of the theoretical predictions, the piezoelectric field in core shell nanowires has rarely been the subject of experimental work. A short overview of the previous work is given in the following. Satish Rai et al. [7] used the piezo-phototronic effect in core shell nanowires to enhance photodetectors. They embedded NWs in a thin polyester film on a silver foil and found increasing resistance and photocurrents with larger mechanical stress on the wires. The work of Pengbo Liu [8] demonstrated the possibility of bandgap engineering using strain. The latter investigated long conical / tapered indium arsenide cores surrounded by a thin indium phosphide shell (see figure 1.3). The strain along the wire is connected to the thickness of core and shell

and manipulates the bandgap. By contacting both ends of the nanowire, they

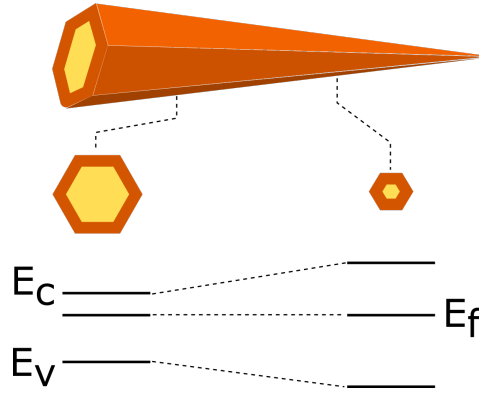


Figure 1.3: a) Change of the conduction and the valence band depending on the ratio of the InAs core (gold) to the InP shell (orange); figure adapted from reference [8].

found high electron mobilities up to $22\,300\text{ cm}^2\text{ V}^{-1}\text{ s}^{-1}$ at room temperature. The group explained the improvement with surface passivation of the InAs cores and the built-in piezoelectric field induced by strain. However, they were not able to isolate the piezoelectric effect and prove the existence of the field. Neither did they show how strongly the field influences the mobility and the resistance of the wire. However, a careful investigation and isolation of the piezoelectric effect is needed to design devices such as semiconductor solar cells. This is the motivation behind the present project.

The basic idea of the project is to isolate the piezoelectric effect and to measure its influence on the electronic properties of III-V semiconductors. To achieve this, the following steps have to be taken: (i) a heterostructure that most likely exhibits strong piezoelectric fields has to be found and defined, (ii) the obtained heterostructure needs to be manufactured, and (iii) the piezoelectric field or a direct ramification of it needs to be isolated and measured. The present report is structured in the same way. The next chapter (chapter 2) discusses strained heterostructures in theory and adumbrates promising structures for practical measurements. Chapter 3 contains information about growth and qualitative outcomes and, last but not least, the careful analysis of the samples as well as its discussion can be found in chapter 4. After that, an outlook will address the open questions in this work.

Chapter 2

STRAINED HETEROSTRUCTURES

2.1 Qualitative model of strained heterostructures

An object consisting of two chemically different structures connected to each other is called heterostructure. The specialty of a heterostructure is the common interface that merges the two structures. This interface can be created in a deposition of one species on the surface of another. The first monolayer in this process will adapt to the chemical environment of the surface and take over its structure. The more layers assemble, the greater the disadvantage of deformed bonds in the top material becomes. Far from the interface, the stress-free state of the top material will be reached by plastic relaxation. In between those poles, the top structure will be strained. An illustration of the described model can be found in figure 2.1. If the bottom structure is not rigid, both structures will have to find a compromise at the interface to balance the forces of their bulk parts. The following conclusions can be drawn from this model:

1. The extent of each layer in the heterostructure will determine its ability to accommodate strain.
2. The amount of strain will depend on the ratio of the interface area to the bulk volume,

3. the cross section area of each component, and
4. the difference of the lattice constants at the interface, called the lattice mismatch.

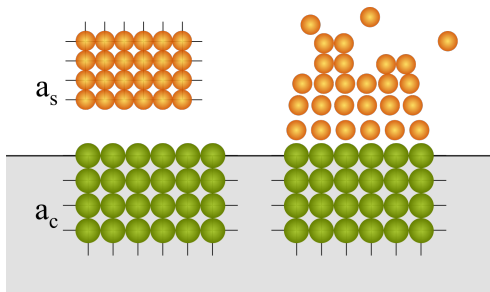


Figure 2.1: Schematic heterostructure consisting of two materials with different stress free states.

Any crystal structure with a non-centrosymmetric unit cell exhibits piezoelectric polarization when it is strained [7]. This local polarization then adds up over the crystal-extent and creates a piezoelectric field. With the aim to measure the piezoelectric field in nanoscale heterostructures, the sample should exhibit unrelaxed strain. Following the four strain criteria above, core-shell nanowires seem to be a good choice. First, they can accommodate large amounts of strain, due to their high aspect ratio of the diameter to the nanowire side and their small dimensions. Secondly, they have a high surface/interface to volume ratio. Thirdly, the growth of core-shell nanowires is flexible and would allow control of the crystal volume ratio. Fourthly, it is possible to introduce ternary components, which offer control over lattice constants and therefore strain by changing the composition.

In this project the two material systems indium arsenide (InAs) on indium phosphide (InP) and indium gallium arsenide ($\text{Ga}_x\text{In}_{1-x}\text{As}$) on InP are examined. InP has a suitable bandgap for solar cell applications [3] and is therefore a suitable material for the outlook of this project. The ternary component $\text{Ga}_x\text{In}_{1-x}\text{As}$ can adopt lattice constants larger than ($x < 0.47$), smaller than ($x > 0.47$), and matched to ($x = 0.47$) InP. Therefore the same material system allows positive, negative and no strain. This property will make it easier to isolate the piezoelectric from other effects. The het-

erostructure consisting of InP and InAs serves as a reference, due to its fixed mismatch.

The crystal structure of all three materials is zincblende in the bulk material. High surface to volume ratios, however, can shift the thermodynamic equilibrium to the similar wurtzite structure. The reason for that shift is still under debate [9-11]. InP [12], $\text{Ga}_x\text{In}_{1-x}\text{As}$ [13], and InAs [10] nanowires were already grown in the wurtzite structure.

So far, a simple model of heterostructures has led to a qualitative choice of the material systems and rough shape of the heterostructure. The result are core-shell nanowire with InP in the core and $\text{Ga}_x\text{In}_{1-x}\text{As}$ or InAs in the shell. In order to complete the heterostructure design, also a quantitative relation between the heterostructure proportions and strain is needed. The strain can then be connected to the piezoelectric properties and a sound prognosis can be made for the growth samples.

2.2 Quantitative model of strained heterostructures

Appendix A contains a detailed description of the strain calculus used in this work. All calculations are based on analytical expressions from the work of Ferrand [14] and Boxberg [4]. The model describes radial heterostructures with cylindrical symmetry and translational invariance along the main axis, resulting in infinitely long nanowires. The latter does not harm the validity of the result, since any segment separated from the ends by a distance more than the nanowire diameter is described correctly (Saint Venant's principle). The crystal structure is either wurtzite or zincblende. Their orientation is chosen in a way that the direction of highest polarization is aligned with the main axis of the heterostructure. Local polarizations can then add up over large distances and create a strong dipole [4]. The direction with the highest polarization is [0001] in wurtzite and [111] in zincblende crystals [14]. The mismatch parallel and perpendicular to the interface is fully accommodated by elastic strain. To stabilize the interface and surface, stress is equal on both sides of the interface and is set to zero at the surface. Analytical expressions

for the main elements of the strain tensor can be found in equations 2.1.

$$\begin{aligned}
\epsilon_{zz}^c &= \frac{(1-\eta)\chi}{\eta+(1-\eta)\chi} f_{\parallel} \\
\epsilon_{zz}^s &= \frac{-\eta}{\eta+(1-\eta)\chi} f_{\parallel} \\
\frac{\epsilon_{\theta\theta}^c - \epsilon_{rr}^c}{2} &= 0 \\
\frac{\epsilon_{\theta\theta}^s - \epsilon_{rr}^s}{2} &= B_s \frac{r_c^2}{r^2} \\
\frac{\epsilon_{\theta\theta}^c + \epsilon_{rr}^c}{2} &= \frac{(1-\eta)\chi}{\eta+(1-\eta)\chi} (f_{\perp} + B_s) \\
\frac{\epsilon_{\theta\theta}^s + \epsilon_{rr}^s}{2} &= \frac{-\eta}{\eta+(1-\eta)\chi} (f_{\perp} + B_s)
\end{aligned} \tag{2.1}$$

The letter f defines the mismatch, $\eta = r_c^2/r_s^2$ marks the ratio of the cross section areas, and the variables B_s and $(f_{\perp} + B_s)$ are functions of the elastic constants c_{ij} , of the lattice mismatch and the ratio η . B_s and $(f_{\perp} + B_s)$ can be found in the appendix (A.8 and A.11) for wurtzite and zincblende crystals. A uniform lattice mismatch ($f_{\parallel} = f_{\perp} = f$) is assumed for zincblende crystals, due to their cubic structure. The calculation of strain is correct for wurtzite along [0001] and a very good approximation for zincblende along [111] [14].

Piezoelectric polarization along the main axis (P_z) can be described using the piezoelectric constants e and the relevant strain components ϵ_{zz} and $(\epsilon_{rr} + \epsilon_{\theta\theta})$ for wurtzite or $(2\epsilon_{zz} - \epsilon_{yy} - \epsilon_{xx})$ for zincblende (see equation 2.2). The piezoelectric field in equation 2.3 is the average effective surface charge density $\langle \rho_s^{pz} \rangle$ divided by the average electrical permittivity $\langle \epsilon \rangle$ [4].

$$\begin{aligned}
P_z^{wz} &= e_{31}(\epsilon_{rr} + \epsilon_{\theta\theta}) + e_{33}\epsilon_{zz} \\
P_z^{zb} &= \frac{e_{14}}{\sqrt{3}}(2\epsilon_{zz} - \epsilon_{yy} - \epsilon_{xx})
\end{aligned} \tag{2.2}$$

$$E_z = \frac{\langle \rho_s^{pz} \rangle}{\langle \epsilon \rangle} = -\frac{P_{z,c}A_c + P_{z,s}A_s}{\epsilon_0(\epsilon_c A_c + \epsilon_s A_s)} \tag{2.3}$$

with the cross section areas for core and shell A_c and A_s , the components of the strain tensor ϵ_{kl} , the electrical permittivity in the core and the shell ϵ_c and ϵ_s , and the vacuum permittivity ϵ_0 . All constants used in the calculations can be found in table 2.1. It should be noted that the permittivity constants

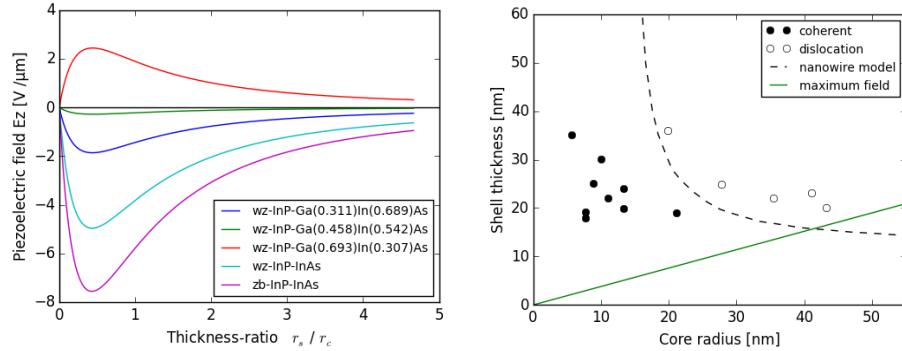
Table 2.1: Physical and electrical properties of GaAs, InAs, and InP in their wurtzite and zincblende phases.

Parameters	GaAs		InAs		InP	
	WZ	ZB	WZ	ZB	WZ	ZB
$a[\text{\AA}]$	3.986[15]	5.6533[16]	4.2742[17]	6.0583[16]	4.1423[18]	5.8687[16]
$c[\text{\AA}]$	6.581[15]		7.0250[17]		6.8013[18]	
$c_{11}[GPa]$	147.6[19]	124.2[19]	99.1[20]	80.3[20]	116.7[20]	98.4[20]
$c_{12}[GPa]$	46.0[19]	51.4[19]	43.6[20]	43.3[20]	50.9[20]	45.4[20]
$c_{13}[GPa]$	33.4[19]		31.9[20]		38.2[20]	
$c_{33}[GPa]$	160.2[19]		114.5[20]		135.9[20]	
$c_{44}[GPa]$	42.4[19]	63.4[19]	22.0[20]	36.9[20]	27.0[20]	39.5[20]
$\epsilon_{14}[C/m^2]$		0.21[21]		-0.050[22]		0.060[22]
$\epsilon_{31}[C/m^2]$	-0.17[5]		-0.081[20]		-0.026[20]	
$\epsilon_{33}[C/m^2]$	0.32[5]		0.012[20]		0.091[20]	
ϵ_{11}	12.9[16]	12.9[16]	14.5[22]	14.5[22]	13.9[22]	13.9[22]
ϵ_{33}	12.9[16]		14.5[22]		13.9[22]	

ϵ_r of zincblende crystals were used for wurtzite, since there are no values for the latter available. All values for the ternary component $\text{Ga}_x\text{In}_{1-x}\text{As}$ were extracted by linear extrapolation between GaAs and InAs (Vegards rule).

The ratio $\eta = r_c^2/r_s^2$ has a strong influence on the strain of the system (compare equation 2.1). In figure 2.2a the piezoelectric field is shown for different ratios of the shell thickness to the core radius. The average extremum of the curves is found at a ratio of 0.43, which means that the core radius should be approximately twice as large as the shell radius to obtain the maximum field strength. For the two structures with InAs shells, zincblende exhibits higher fields. This is due to the fact that the graph shows the isolated field of the z -direction. Contributions from the other strain component are omitted (see equation 2.3). This restriction affects wurtzite and zincblende crystals in an opposite way, compared to numerical calculations provided in reference [4]. The ladder solution shows that in fact wurtzite exhibits higher fields. The piezoelectric field in the analytical solution will be underestimated in wurtzite and overestimated in zincblende crystals, due to the contribution of strain components perpendicular to the main axis. The analytical results are in good agreement with reference [4]. When the Gallium fraction is increased, the mismatch to InP shrinks and the effective strain decreases together with the piezoelectric field. At $x = 0.46$ the shell is close to the lattice match and the field almost disappears. For compositions exceeding 0.47, the strain and the field are reversed.

After clarifying the relative relation core radius and shell thickness, the absolute radius of the heterostructure needs to be discussed. An important



(a) The Piezoelectric field in InP-Ga_xIn_{1-x}As core-shell nanowires in the wurtzite ($0 \geq x \geq 0.693$) and zincblende phase ($x = 0$) against the ratio of the shell thickness to the core radius. (b) InAs-InP core-shell heterostructures: critical shell thickness as a function of core radius; the dashed line represents the calculated critical dimensions and the circles mark experimental findings; data is from reference [23]; the ratio creating the maximum field is 0.38 (green line).

Figure 2.2: Analysis of the piezoelectric field depending on the relative shell thickness in InP-Ga_xIn_{1-x}As core shell nanowires (left) and of the critical absolute dimensions in InAs-InP core-shell nanowires.

restriction on the choice of dimensions for the heterostructure will be the critical thickness, which marks the limit of elastic strain and the onset of relaxations. To be more precise, there is a critical core radius R_c and a critical shell thickness H_c , below which no dislocations appear. Possible plastic relaxations are first the straight edge dislocations parallel to the nanowire axis and secondly the edge dislocation loops, which are normal to the nanowire axis [24]. Salehzadeh et al. [23] calculated the onset of dislocation in wurtzite InAs-InP core-shell nanowires oriented in [0001]. The mismatch in such a heterostructure amounts to 3.3%. Figure 2.2b shows their result with good agreement with experimental data. The optimal ratio for an optimized piezoelectric field in InAs-InP core-shell wires was found to be 0.38 in the present work and was added to figure 2.2b. Although the calculation of Salehzadeh et al. do not consider exactly the same heterostructures as this work, both can be assumed to behave very similarly [24]. Structures with less mismatch, like the ones with the shell material Ga_xIn_{1-x}As, would exhibit a similar line shape and allow larger critical parameters. It should be noted, that the calculations of critical dimensions in core-shell nanowires are quite discrepant. The critical core radii of Salezadeh et al. are relatively large (ten times

larger) compared to findings in other references [24].

The quantitative analysis has shown that wurtzite core-shell heterostructures oriented in [0001] can exhibit relatively large piezoelectric fields in the order of 10^6 V m^{-1} . A calculation of the ideal ratio from the shell thickness to the core radius yielded 0.43 for the heterostructures in the present work. For the large mismatch of 3.3% in InP-InAs core-shell nanowires, dislocations and relaxation of strain play a major role in nanowires with large diameters.

Chapter 3

GROWTH

The prerequisite for a successful measurement is a proper sample. The aim of this chapter is to describe a growth process to manufacture the heterostructures described above. First, the wanted requirements are summarized, then conclusions for the growth process are drawn. Wurtzite indium phosphide (InP) was chosen to be the core material and gallium-indium-arsenide ($\text{Ga}_x\text{In}_{1-x}\text{As}$) or InAs ($x = 0$) the shell material. The growth direction and therefore the main axis of the nanowire is oriented along [0001]. Strain and therefore the piezoelectric field depend on the mismatch at the interface and on the relative core and shell thickness. Dislocations and successive strain relaxation occur for thicker nanowires and demand a control of the total diameter. What can be concluded for the growth process?

1. The growth conditions need to favor nanowire growth instead of planar growth.
2. The substrates' surface should be either $\langle 111 \rangle\text{A}$ or $\langle 111 \rangle\text{B}$ in order to determine the growth direction and main axis of the nanowires along [0001].
3. The composition of $\text{Ga}_x\text{In}_{1-x}\text{As}$ and the relative thickness of the core and the shell will determine the strain. Therefore those factors need to be controlled in the growth process.
4. A thin layer can accommodate more strain than a thick layer. The parameter of absolute diameter needs to be adjustable in order to avoid strain relaxation.

Those requirements are the objectives for the two experimental approaches of this work. The next three sections will describe their concept and development in great detail.

3.1 Metal Organic Vapor Phase Deposition

Metal-organic vapor phase deposition (MOVPE) is a very flexible and versatile growth technique and is able to produce almost all group III / V semiconductors. It allows growth of high purity materials [25] and abrupt interfaces [26]. Further, MOVPE is a scalable growth technique, which is particularly interesting for the development of solar cell prototypes, which is a possible outlook for this project. All samples were grown in a MOVPE machine produced by the Swedish company Epiquip.

All experiments of the present work were carried out at a pressure of 100 mbar and a temperature between 510 °C and 750 °C. Low pressures have the benefit of reducing parasitic reactions of the precursors and enhance the mass transport. The temperature range mentioned above falls mainly in the mass transport limited regime, which is normally defined between 550 °C and 750 °C [26].

The core material InP was grown with the precursors Trimethylindium (TMIn) and Phosphine (PH₃) and the shell material Ga_xIn_{1-x}As with TMIn, Trimethylgallium (TMGa) and Arsine (AsH₃). All precursors were carried in a flow of hydrogen (H₂) with a flow-rate of 6000 sccm/ min. Such high gas velocities reduce parasitic reactions, contribute to efficient use of precursors, and enable instantaneous changes of gas composition, which can be used for producing sharp interfaces [26]. The use of hydrogen has the benefit of being almost free from impurities, which reduces impurity incorporation in the solid. Furthermore, hydrogen disarms methyl radicals and forms relatively inactive methane molecules with them. At temperatures higher than 300 °C, the precursor gases phosphine or arsine were additionally used as a protective gas.

The choice and preparation of the substrate determines the growth direction and nucleation sites. In the present work, zincblende InP wafer with the orientation $\langle 111 \rangle$ A or $\langle 111 \rangle$ B were used, so that the growth direction of the nanowire is oriented along the hexagonal direction [0001]. Depending on the growth mode, one of the two orientations (A or B) is chosen. For gold-seeded growth or vapor-liquid-solid growth (VLS), the orientation $\langle 111 \rangle$ B

was used, which is common in literature [27-29]. In VLS growth mode, the nanowire growth is catalyzed by a liquid gold nanoparticle [9]. The gold nanoparticle serves as a catalyst for axial growth and provides good control of axial heterostructures. However, the seed particle strongly favors the axial growth, which complicates the growth of radial heterostructures. In contrast, selective-area epitaxy (SAE) does not need any catalyst particles. The crystal nucleates directly on the substrate. To prevent planar growth, the substrate is covered with a mask, which restricts nucleation to the non-covered areas of the mask. This growth mode prefers the $\langle 111 \rangle$ A orientation [12, 30-31]. The following two sections provide a closer look at each growth mode and their use in the project.

3.2 Gold seeded growth

In an aerosol process, gold nanoparticles were deposited on an InP $\langle 111 \rangle$ B wafer with a resulting density of one per square micrometer on average. The diameters of the seed particles were distributed around 20 nm or 40 nm, respectively. The wafer with gold nanoparticles on the surface was then sliced into smaller pieces of approximately a quarter square centimeter. The growth process of the core is divided into three phases:

1. The substrate is annealed at a high temperature of 550 °C in an atmosphere of H₂ and PH₃. This desorbs oxides, adatoms and other contaminants.
2. A nucleation phase supersaturates the gold particle with Indium and initiates the growth.
3. Actual growth: In this phase hydrogen bromide (HBr) is added to etch the nanowires in situ to reduce tapering [32].

Based on the findings of Paiman et al. [28], a basic set of growth parameters was selected.

With the settings, shown in table 3.1, and 40 nm gold nanoparticles, slight tapering and pure wurtzite structure was expected. The molar fraction of HBr in the gas phase was varied to obtain an etching rate, which eliminates tapering but does not hinder axial growth too much. Figures 3.1a–3.1c are images of a scanning electron microscope (SEM) by Hitachi (SU 8010, Hitachi Ltd., Tokyo, Japan). They show three samples of InP cores, etched with

Table 3.1: VLS growth parameters

Reactor settings		Technique: MOVPE, chamber pressure: 100 mbar, total flow: 6000 sccm / min, carrier gas: H ₂ , protection gas: H ₂ /PH ₃ or H ₂ /AsH ₃ , substrate: InP(111)B, mean gold nanoparticle diameter: 20 or 40 nm					
Core growth	Temp [°C]	Time [mm:ss]	X _{PH3}	X _{TMI_n}	V/III	X _{HBr}	
Phase 1: Annealing	550	10:00	6.17E-3	-	-	-	
Phase 2: Nucleation	510	00:15	6.17E-3	1.84E-5	335	-	
Phase 3: Core Growth	510	08:00	6.17E-3	1.84E-5	335	4.03E-4	
Shell growth	Temp [°C]	Time [mm:ss]	X _{PH3}	X _{AsH3}	X _{TMI_n}	X _{TMGa}	V/III
Phase 1: Temperature change and partly depletion	510	01:00	6.17E-3	-	-	-	-
Phase 2: Introduction of V-component	510	00:10	-	4.95E-3	-	-	-
					4.08E-6	1.84E-6	836
Phase 3: Shell growth	510	00:14	-	4.95E-3	3.26E-6	2.76E-6	821
					1.63E-6	3.68E-6	932

different molar fractions of HBr. A low molar fraction of $1.1 \cdot 10^{-4}$ (fig. 3.1a) clearly shows strong tapering, while a molar fraction of $7.8 \cdot 10^{-4}$ (fig. 3.1b) resulted in drastic decrease of the growth rate. In between those extremes, a HBr content of $4.0 \cdot 10^{-4}$ (fig. 3.1b) resulted in nanowires with a small base and minor tapering.

However, a large amount of nanowires showed faceted side walls (see inset of figure 3.1b), which indicate zincblende indium phosphide [33]. In order to avoid zincblende nanowires, the average diameter of the gold seeds was changed to 20 nm. As discussed above, the diameter of the nanowire will favor the nucleation of indium phosphide in the wurtzite phase [9]. Indeed, scaling down the gold seeds to 20 nm eliminated nanowires with faceted side walls. The result, grown with the conditions in table 3.1, can be seen in figure 3.1d. The sample serves as a reference to the core in the heterostructure described in the following. The dimensions are given in table 3.2 at the end of this section.

The growth process of the shell is divided into three phases:

1. Temperature-change to the required shell growth temperature in order to overcome limitations to shell growth and partial depletion of the seed particle from indium.
2. Change of the group V-component from PH₃ to arsine (AsH₃).

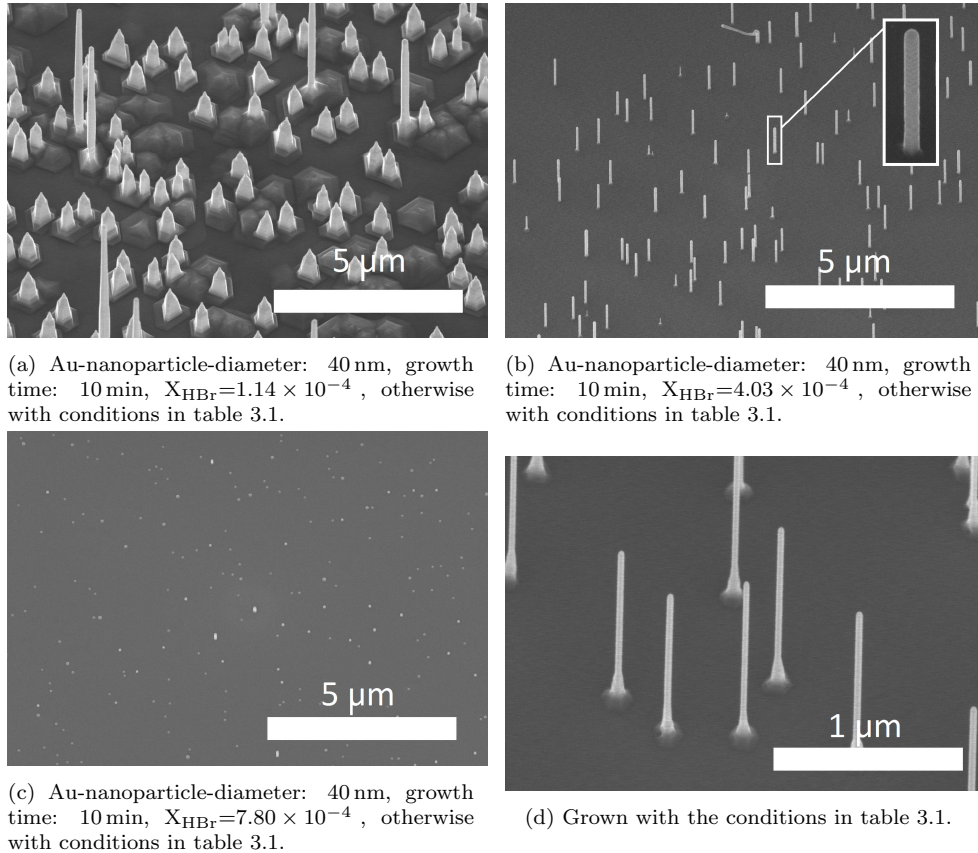
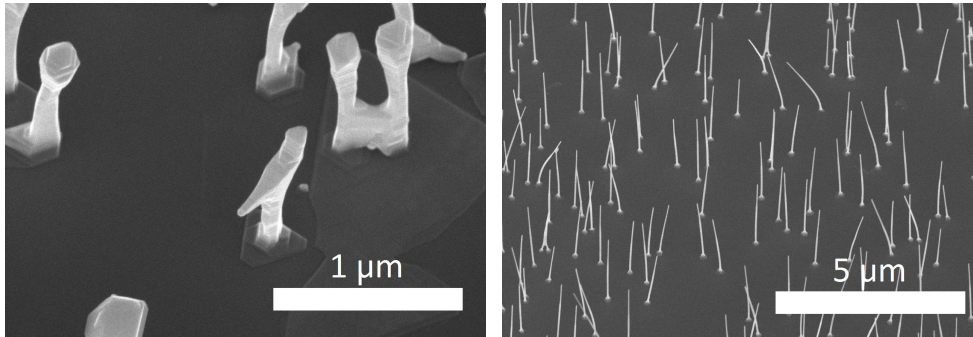


Figure 3.1: (a)-(c) three samples with increasing rates for in-situ etching, (d) core reference for VLS growth samples.

3. Introduction of the group III-components TmIn and Trimethylgallium (TMGa) and actual growth of the shell or an additional axial segment.

Shell growth is usually carried out at higher temperatures, where thermodynamic barriers of binding sites are less important and the growth speed depends less on the crystal direction. If the axial growth rate is dominant in the mid-temperature regime, it will be closer to the radial growth rate in the high-temperature regime. Furthermore, the crystal quality is known to benefit from higher temperatures [26]. The seed particles' sensitivity towards changes in circumambience, however, can complicate the growth of radial heterostructures. In this project, the gold nanoparticle seems to move



(a) Au-nanoparticle-diameter=40nm, 5 min ramp, 540 °C, 1 min stabilization, V-component switched in 15 s, V/III-ratio=411, $X_{TMIn}=1.02E-5$, $X_{TMGa}=1.84E-6$.

(b) Au-nanoparticle-diameter=20 nm, 510 °C, 1 min stabilization, V-component switched in 10 s, V/III-ratio=821, $X_{TMIn}=3.26E-6$, $X_{TMGa}=2.76E-6$.

Figure 3.2: Both cores were grown like the example in table 3.1; figure 3.2a shows shell growth with meandering seed particle, in figure 3.2b most seed particles stayed on top of the nanowire; the tilted nanowires occurred due to the strain in the heterostructure.

or fall off from the nanowire’s tip and create branches or planar tracks on the substrate when growth conditions are changed. It is not the scope of this work to root out the process behind this, but it can be stated that the wetting angle of the seed particle plays an important role in the particle [34]. Especially changes in the composition of the indium-gallium-gold alloy will have an influence on the wetting angle [35]. Hence, depletion of the gold particle during heating and enrichment of the nanoparticle after introduction of the III-components can lead to movements of the seed particle.

A rough mapping of the parameter space suggested the following: it helps to grow the shell at the same temperature as the core. After core growth, the seed particle had one minute to equilibrate, the V-component was switched within a few seconds, and the shell growth was carried out without etching for short times. The growth results before and after optimization are shown in figures 3.2a and 3.2b. At this point, it should be noted, that the previous conclusions about the parameter change are not a result of systematic analysis and can only be interpreted as simple observations. Table 3.1 shows the growth parameters used in this work.

The morphology for the samples relevant to the later analysis is given in table 3.2. All length measurements were taken with the use of scanning elec-

tron microscopy (SEM) images. The scale bar served as a length reference. The nanowire-length was measured along the facing side from the top to the base of the nanowire. Diameters were evaluated by measuring the full width half maximum of an intensity profile perpendicular to the nanowires main axis. Two diameters were averaged - one above the base and one below the end of the shell. This provides the additional information of tapering, which is the difference between the top and the bottom diameter. Negative values mark inverse tapering, where the top is thicker than the bottom. The data provided in 3.2 and 3.4 are mean values of many nanowires in the center of the substrate. The standard deviation of those values is also given for each average. Based on the mean and standard deviation of the (referenced) core and the shell diameter, the strain in core and shell, as well as the piezoelectric field along z were calculated. Values for all possible combinations of core and shell radius were averaged, weighted with the deviation from the mean. The results are given in tables 3.2 and 3.4. It should be noted, that the $\text{Ga}_x\text{In}_{1-x}\text{As}$ composition was not measured. The given values are the molar fraction of Ga divided by the sum of the molar fractions of In and Ga.

Table 3.2: Average morphology of $\text{InP-Ga}_x\text{In}_{1-x}\text{As}$ core-shell nanowires seeded with gold nanoparticles; all samples were grown with the conditions in table 3.1.

Core reference	Length [nm]	Diameter [nm]	Tapering [nm]			
Sample VR	1443 ± 231	39 ± 4	3 ± 3			
Core/Shell samples	$\text{Ga}_x\text{In}_{1-x}\text{As}$	Length [nm]	Diameter [nm]	Tapering [nm]	ϵ_{zz}^c (calc) [%]	E_z (calc) [10^6 V/m]
Sample V1	0.311	2802 ± 258	53 ± 5	-1 ± 3	0.49	-1.61
Sample V2	0.458	2702 ± 415	50 ± 5	-2 ± 4	0.08	-0.21
Sample V3	0.693	2377 ± 345	47 ± 4	-3 ± 3	-0.20	1.26

3.3 Selective area epitaxy

In this growth mode, a mask is needed to restrict the growth to small areas. For this purpose, a 20 nm layer of SiN_x was deposited on an $\text{InP}\langle 111 \rangle \text{A}$ surface. The surface was then covered by a lift-off and imprint resist. A hole pattern was created by a plastic imprint stamp and the structure was thinned down with the use of oxygen plasma until the substrate laid bare. The openings are then used to etch the SiN_x layer with reactive ion etching.

Each hole has an average diameter of 130 nm and a spacing of 1 μm . The array has a hexagonal structure.

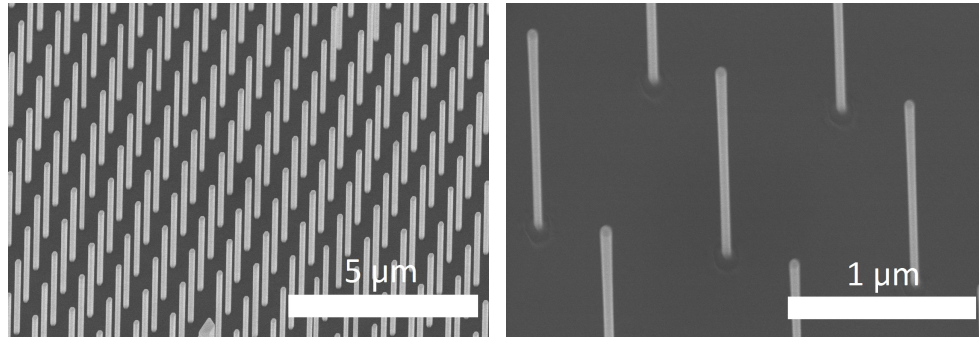
Table 3.3: SAE growth parameters

Reactor settings		Technique: MOVPE, chamber pressure: 100 mbar, total flow: 6000 sccm/min, carrier gas: H_2 , protection gas: H_2/PH_3 or H_2/AsH_3 , substrate: InP(111)A, hole diameter = 130 nm, pattern density: $0.87/\mu\text{m}^2$					
Core growth		Temp [$^\circ\text{C}$]	Time [mm:ss]	X_{PH_3}	X_{TMI_n}	V/III	X_{HBr}
Phase 1: Annealing		750	10:00	2.47E-2	-	-	-
Phase 2: Core Growth		710	10:00	2.47E-2	1.22E-5	2025	-
Phase 3: Etching		620/660	10:00	1.23E-2	-	-	8.28E-5
Shell growth		Temp [$^\circ\text{C}$]	Time [mm:ss]	X_{AsH_3}	X_{TMI_n}	V/III	
Phase 1: Switch of V-component temperature change		460	02:00 - 05:00	5.50E-4	-	-	
Phase 2: Shell growth		460	00:15 - 05:00	5.50E-4	82		

Based on the process of M. Heurlin et al. [31] a growth process was designed (see table 3.3). The core growth is divided into three phases:

1. The substrate is annealed at a high temperature of 750°C in a atmosphere of H_2 and PH_3 . This desorbs oxides, adatoms and other contaminates from the substrates surface.
2. Introducing III-component and growth of nanowires
3. In situ etching with hydrogen bromide and H_2/PH_3 protection gas; in this step the morphology of the nanowire is manipulated.

This process creates an array of uniform and straight InP nanowires with a pure wurtzite structure [31]. The average diameter is 148 nm after ten minutes of growth, which is quite limited in accommodating strain, due to relaxation processes in thick layers. Thus, an etching step was added to the growth process to reduce the core diameter before the shell is grown. The product after phase one and two (table 3.3) is shown in figure 3.3a, the product of phase one to three can be seen in figure 3.3b. It can be clearly seen that the nanowire morphology was changed during etching. Most often, inverse tapering was the resulting change, but often additional features were added to this change. Moreover, the etching rate was varying strongly over



(a) InP cores after phase two of the process shown in table 3.3. (b) InP cores after phase 3 of the process shown in table 3.3.

Figure 3.3: Two nanowire arrays in selective area growth mode; the left shows the nanowires as-grown and the figure on the right hand side shows them after the etching process.

the substrate. Especially when etching down to smaller diameters, nanowires towards the edges of the substrate vanished.

Series with temperature variations and subsequent careful analysis of the etching rates along a radial line from the substrates center did not exhibit a clear correlation between temperature and etching rate. Towards smaller diameters, the etching rate increases rapidly, due to a heterogeneous reaction on the surface with the rate limiting step. This would suggest, that etching is quicker with a higher surface to volume ratio.

Instabilities of the etching process over the substrate would not directly influence the quality of electrical measurements. The nanowires can be picked selectively from a small area of the substrate, as described in section 4.1.1. The changes in morphology between the individual nanowires in a small area is a bigger concern, because they will be hidden under the shell of the heterostructure. In samples with nanowires etched down to about 40 to 60 nm in diameter, the standard deviation can be up to 12 % of the diameter (see table 3.1). Before the etching process, the standard deviation of the diameters amounts to about 3 % of the total diameter. Since the fluctuation of the shell thickness and its dependency on the core diameter is unknown, it will be difficult to reconstruct the proportions of a single heterostructure. Furthermore, it is barely possible to measure the diameter of the core when it is covered by a shell. This means, that the fluctuation should be as low as

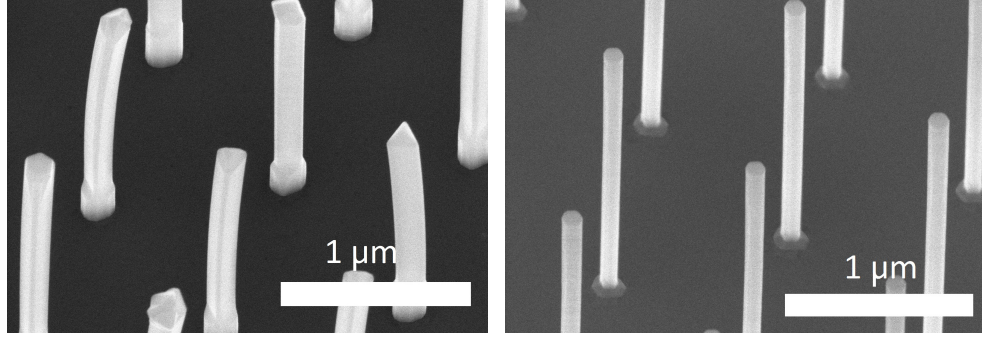
possible to simplify the analysis. Moreover, in-situ etching could influence the surface structure and the epitaxial growth of the shell.

Another approach to diminish the diameter of the nanowires is the modification of the growth mask. This would reduce large diameter fluctuations and ensure epitaxial core surfaces. Instead of the imprint method, electron beam lithography (EBL) was used to produce the mask. The hole diameter of the samples was reduced to 50 nm. Unfortunately, the growth with the newly prepared masked substrates was not completed before the end of this project. It will be mentioned in the outlook section, chapter 5.

The InGaAs shell is as well part of the outlook section, but the simpler heterostructure with the binary component indium arsenide (InAs) was actually grown. The binary structure has defined lattice parameters, which simplifies the measurement of strain with techniques like x-ray diffraction. The shell part was grown in two phases:

1. Switch of the V-component and changing to the desired temperature (see table 3.3); both is changed simultaneously.
2. Actual growth of the shell by introduction of the III-component.

In this way, various core shell nanowires with a fixed core growth and varying InAs shell growth times were produced. The morphology of the important ones for the next chapter about electrical measurements are summarized in table 3.4. The length measurements and calculations follow the same procedure described above. Two different core references are used. Sample SR1 has an etching temperature (phase 3 of the core growth - see table 3.3) of 620 °C and sample SR2 was etched at 660 °C. On top of those core references, the shells were grown for different duration. The values are 300 s for S1, 60 s for S2, and 20 s for S3. SEM images of the two samples S1 and S3 are shown in 3.4a and 3.4b. The nanowires of sample S1 are tilted, which can be caused by the strain in the structure.



(a) Growth according to table 3.3; the etching temperature was 620 °C and the shell growth-time was 300 s.

(b) Growth according to table 3.3; the etching temperature was 660 °C and shell growth-time was 20 s.

Figure 3.4: Two SEM images of InP-InAs core-shell nanowires with different shell thickness.

Table 3.4: Average morphology of InP-InAs core-shell nanowires grown by SAE; all samples were grown with the conditions in table 3.3.

Core references	Length [nm]	Diameter [nm]	Tapering [nm]		
Sample SR1	1938 ± 163	49 ± 6	8 ± 2		
Sample SR2	1037 ± 389	54 ± 4	10 ± 2		
Core/Shell (ref)	Length [nm]	Diameter [nm]	Tapering [nm]	ϵ_{zz}^c (calc) [%]	E_z (calc) [10 ⁶ V/m]
Sample S1 (SR1)	1968 ± 127	170 ± 11	-10 ± 4	3.21	-0.43
Sample S2 (SR1)	2161 ± 60	99 ± 9	-22 ± 15	2.34	-3.73
Sample S3 (SR2)	2390 ± 51	105 ± 3	-9 ± 4	2.30	-3.94

Chapter 4

ELECTRICAL MEASUREMENTS

4.1 Experimental details

4.1.1 Device fabrication

The goal is to contact a single nanowire with defined contact positions. The starting point are nanowires standing on the top of a substrate. The nanowires were then transferred with a sharp tip of a cleanroom-tissue onto a device template (see figure 4.1a). Device templates provide the infrastructure for connecting macroscopic with nanoscale contacts. It consists of a silicon wafer covered with a silicon oxide layer of 100 nm and measures $3\text{ mm} \times 5\text{ mm}$. On top of that, a gold pattern connects the inner contact fields with larger ones placed on the outside. A vertical array of contact fields lies in the center of the device template. Each contact field is $100\text{ }\mu\text{m} \times 100\text{ }\mu\text{m}$ wide and provides a fine dot grid, marks, and crosses for alignment purposes in the following process (see figure 4.1b).

If placed correctly, the nanowires lay inside the contact fields. To identify a single intact wire and its coordinates on the grid, SEM images were recorded of each field and nanowire position. An example is shown in figure 4.1b. With help of a Matlab script, provided by David Göransson, a contact design file was produced, which places four contacts on the chosen nanowire in each field. The device was then spincoated with 520 nm of the resist poly(methyl-methacrylate) (PMMA) and heated to $180\text{ }^\circ\text{C}$ for 10 min. The contact design was then engraved into the resist by a electron beam

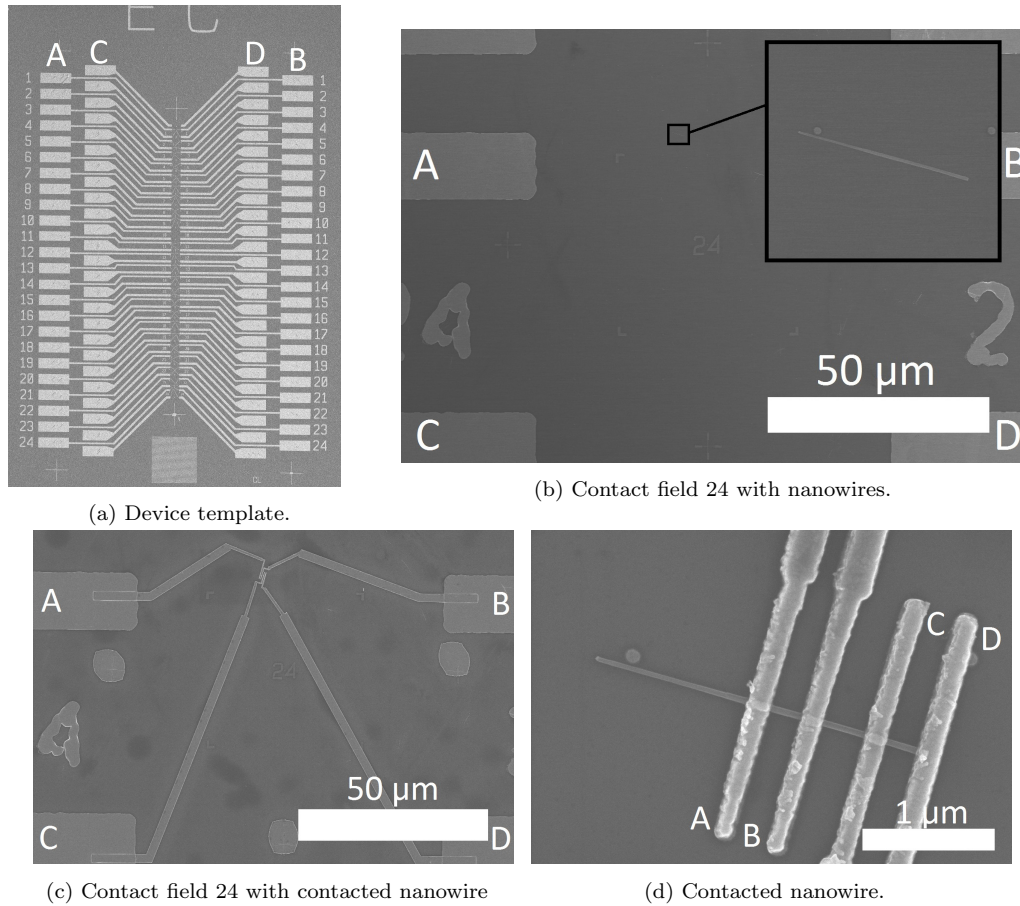


Figure 4.1: Two SEM images of the device template (4.1a) with nanowires on the contact fields (4.1b).

lithograph (Raith 150, Raith GmbH, Dortmund, Germany). The acceleration voltage was either 10 kV or 20 kV and the area dose was $270 \mu\text{A s cm}^{-2}$. After exposure, the gravure was developed for 90 s in a mixture of three parts isopropanol and one part MIBK (Microchem), followed by 60 s in pure isopropanol. The device was then etched in oxygen plasma (Plasma Preen II-862, Plasmatic Systems Inc., North Brunswick, NJ, United States) for 30 s to reduce organic contamination on the surface. In order to remove potential oxides on the nanowire surface [36], the sample was etched at 42°C in a solution of 10 mL deionized water and 0.127 mL NH_4S_x solution (consisting of a

20 % $(\text{NH}_4)_2\text{S}$ stock solution from VWR International mixed with elemental sulfur). The samples were etched for 5 min, rinsed with deionized water, dried in a stream of nitrogen, and quickly transferred to the evaporation chamber (AVAC AB, Linköping, Sweden). The etching process was evaluated by the contact resistance only, which is discussed below. At a vacuum lower than 5×10^{-7} mbar, nickel was evaporated at approximately 1.5 \AA s^{-1} to a layer thickness of 30 nm layer and gold was evaporated at rates increasing from approximately 1.5 \AA s^{-1} to 6.5 \AA s^{-1} , forming a layer thickness of 100 nm. After metal deposition, the sample was placed in the Microposit Remover 1165 (DOW Chemical Company) at $80 \text{ }^\circ\text{C}$ for 30 min to dissolve the PMMA resist under the evaporated metal. This process disconnects the metal layer from the device template and it can be lifted off. The contact design, which is directly in contact with the device template, remains. The result can be found in figure 4.1c and 4.1d. Electrical measurements were performed in the time span of maximum 8 h after the lift-off process.

4.1.2 Electrical measurements on individual nanowires

All measurements were performed on a Model 4200 - Semiconductor Characterization System produced by the company Keithley (Tektronix Inc., Beaverton, OR, United States) connected to a Source One probe station (Cascade Microtech Inc., Beaverton, OR, United States). The current and voltage specifications of the tool can be found in table 4.1. For all measurements the automated mode was used, so that the tool was able to react on the measured data and adjust the current and voltage ranges accordingly (compare table 4.1). This can lead to discontinuity in the curves, but provides higher accuracy in each section and the tool can adjust to large changes in the current, which occurred frequently. Every nanowire has 4 contacts, named A, B, C, and D. The contact closest to the top of the nanowire is defined as contact A and the naming follows the alphabetic order towards the bottom of the nanowire (compare figure 4.1d). The contacts to the nanowire are linked via the contact pattern on the device template to the outer gold plates (compare figure 4.1a), which can be contacted by probe needles.

A measurement of the current voltage relation (I-V) was performed on pairs of nanowire contacts. In this work, the combinations A-B, B-C, and C-D were probed. To reduce influences of the needles, all combinations were measured with the same two probe needles. The I-V curves were recorded by sweeping the bias voltage and measuring the current in one of the contacts.

Table 4.1: Specifications of the Semiconductor Characterization System, Model 4200, from the manufacturer Keithley; all data is from the manual of the measurement system.

Currents		Measure			Source	
Current Range	Max. Voltage	Resolution	Accuracy $\pm(\%rdg + amps)$	Resolution	Accuracy $\pm(\%rdg + amps)$	
100 mA	21 V	100 nA	0.045 % + 3 μ A	5 μ A	0.050 % + 15 μ A	
10 mA	210 V	10 nA	0.037 % + 300 nA	500 nA	0.042 % + 1.5 μ A	
1 mA	210 V	1 nA	0.035 % + 30 nA	50 nA	0.040 % + 150 nA	
100 μ A	210 V	100 pA	0.033 % + 3 nA	5 nA	0.038 % + 15 nA	
10 μ A	210 V	10 pA	0.050 % + 600 pA	500 pA	0.060 % + 1.5 nA	
1 μ A	210 V	1 pA	0.050 % + 100 pA	50 pA	0.060 % + 200 pA	
100 nA	210 V	100 fA	0.050 % + 30 pA	5 pA	0.060 % + 30 pA	
Voltages		Measure			Source	
Voltage Range	Max. Current	Resolution	Accuracy $\pm(\%rdg + volts)$	Resolution	Accuracy $\pm(\%rdg + volts)$	
200 V	10.5 mA	200 μ V	0.015 % + 3 mV	5 mV	0.02 % + 15 mV	
20 V	105 mA	20 μ V	0.01 % + 1 mV	500 μ V	0.02 % + 1.5 mV	
2 V	105 mA	2 μ V	0.012 % + 150 μ V	50 μ V	0.02 % + 300 μ V	
200 mV	105 mA	1 μ V	0.012 % + 100 μ V	5 μ V	0.02 % + 150 μ V	

A bias voltage is applied on both contacts with the same absolute value but different signs. During the measurement, the voltage bias is changed symmetrically towards each other until the opposite end is reached. In a contact pair X-Y, contact X is defined to start from negative bias voltage. This means that the contact combinations A-B and B-A would start from opposite bias conditions. An example for a characteristic I-V curve is given in figure 4.2.

The resistance and the rectification were extracted from the measured I-V curves. To that end, the differential resistance $R_{diff} = dV/dI$ was calculated using a noise robust differentiator proposed by Pavel Holoborodko [37] (equation 4.1).

$$f'(x^*) \approx \sum_{k=1}^M \frac{f_k - f_{-k}}{x_k - x_{-k}} \cdot 2k \quad (4.1)$$

While x is the current, f is the total bias voltage difference between the two contacts, k gives the distance to the center point, and $M = 2$. The six values for the differential resistance closest to zero bias voltage were averaged and the result was taken as the resistance of the measurement.

The absolute current difference between pairs with the same absolute bias voltage give the absolute rectification. The absolute rectification relative to the current at positive bias voltage, gives the relative rectification. In

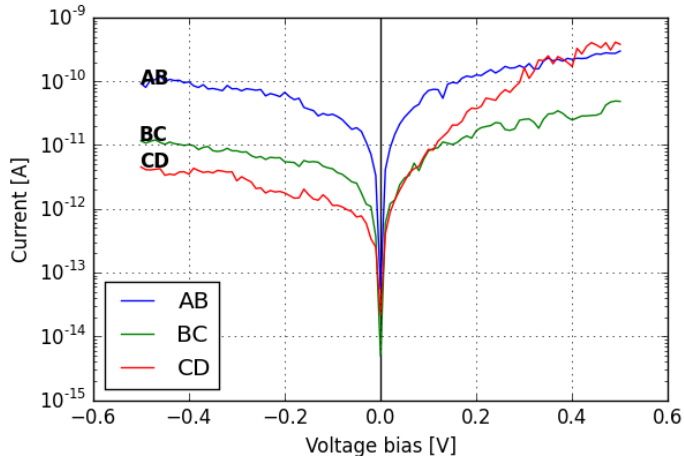


Figure 4.2: Exemplary current voltage characteristic of the sample V2; all contacts exhibit positive absolute rectification or a relative rectification larger than one.

any contact pair X-Y, positive values (absolute rectification) or values above unity (relative rectification) mark higher currents for positive bias voltage on contact X. Rectifications were evaluated between 0.15 V and 0.35 V total bias voltage and the obtained values were averaged.

4.1.3 Morphology of individual nanowires

Additionally to the electrical measurements, detailed SEM images, like the one in figure 4.1d, provided information about the contact width, the distance between the contact and the width of the nanowire in the middle between two contacts. The measurement procedure is described in section 3.2. Measurements on the core diameter inside a core-shell nanowire can not be measured in a simple manner. In the following it is described how to infer the core diameter from the outer diameters of the heterostructure. The samples V1-3 have a top segment originating from the shell growth phase (compare figure 4.1d). The growth of the top segment was catalyzed by the same seed particle as the core, which is hidden under the shell. For a given wetting angle of the gold seed particle during growth, the diameter of the wire is correlated with the volume of the seed particle [38]. Thus, the mean diameter will vary for different growth conditions, but the diameter distribution will depend only

on the volume distribution of the seed particles and remains constant. Table

Table 4.2: Diameter relation between core reference and top part of the samples V1-3.

Sample	Core Reference	V1	V2	V3
Mean diameter at top [nm]	36	33	32	32
Core-to-top offset [nm]		+3	+4	+4
Standard deviation [nm]	2.8	2.6	2.5	2.9

4.2 shows the statistics for the diameter of the top part close to the seed particle and the top part of the reference core. It is clearly visible from the table, that the standard variation of the samples and the core is very similar. Therefore it is reasonable to assume that there is a direct correlation between the core thickness and the top part of an individual nanowire. The offset is simply the difference between the mean diameter of the reference core and the mean diameter of the samples top part. Assuming the core is uniform in diameter, this creates the opportunity to infer the shell thickness from the outer diameter. This is, however only possible for the VLS samples V1, V2, and V3.

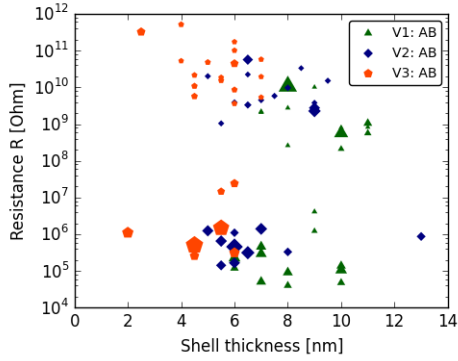
4.2 Results and Discussion

4.2.1 Gold seeded $\text{Ga}_x\text{In}_{1-x}\text{As-InP}$ core-shell nanowires

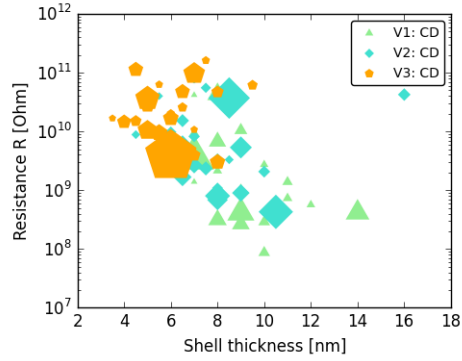
Resistance is known to depend on the contact distance (d), the cross section area (A), and the resistivity of the material (ρ):

$$R = \frac{\rho d}{A} \quad (4.2)$$

Influences on the distance and the shell thickness are evaluated first. The contact pairs A-B and C-D have a mean distance of 217 nm - 222 nm with a standard deviation ranging from 11 nm to 16 nm. Therefore, the distance has a minor influence on the resistance in those contacts. Figures 4.3a and 4.3b show the resistance of A-B and C-D as a function of the shell thickness, which was calculated as described above. The size of the markers reflects the relative rectification. In the A-B measurements (figure 4.3a), the markers are split into two groups, while the group with lower resistances (A1) has a relative rectification larger than unity (= size shown in the legend) with



(a) Dependence of the resistance on the shell thickness in A-B; the color and shape marks different samples, the size reflects the relative rectification (legend shows size with no rectification).



(b) Dependence of the resistance on the shell thickness in C-D; the color and shape marks different samples, the size reflects the relative rectification (legend shows size with no rectification).

only a few exceptions. In the C-D measurements (figure 4.3b), all markers are in the group with high resistances and their rectification seems to spread randomly in both directions with strong individual rectifications. In both figures, the resistance seems to exponentially decrease with increasing shell thickness. However, a concrete relation can not be extracted from the figures, due to the data scattering larger than two orders of magnitude. Moreover, the shell thickness decreases with increasing gallium fraction.

In between the contacts B and C, the distance can vary from 50 nm to 680 nm. A colored map of the resistance in dependence on shell thickness and contact distance is shown in figure 4.4. The strong dependence on the shell thickness can also be observed following horizontal lines of equal shell thickness. However, the graph does not show a clear relation between the contact distance and the resistance.

A statistical overview of the obtained rectifications can be found in table 4.3. It shows which part of the samples (count) had positive or negative rectification, meaning high currents with a positive or negative bias voltage on contact X in X-Y. The mean value of the relative and absolute rectification is also given. Due to the splitting of the results in figure 4.3a, also the rectification data was split into the group with low (A1) and high (A2) resistances. The relative amount of samples with a certain rectification (compare the count columns in table 4.3) follow a similar trend in all samples. An exception is B-C in sample V2.

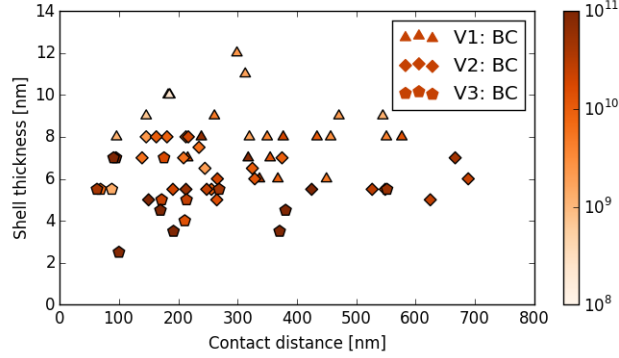


Figure 4.4: Dependence of the resistance on the shell thickness in B-C; the color provides the resistance, the shape different samples and the position determines the shell thickness and contact distance.

Additional data in table 4.3 gives the rectification for a contact pair E-F on the top part of the nanowire. Note that the naming is an exception to the previous cases, since E-F lies closer to the top of the wire, than A-B. The rectification in those measurements is never negative, meaning that higher currents are obtained for a negative bias on contact E, which lies closer to the top of the wire. Figure 4.5 adds information about the resistance in the top part of the nanowire. The average distance between the contacts E and F is 331 nm, 332 nm, and 258 nm for the samples V1, V2, and V3 (standard deviation for the distances is below 8 nm). The resistances range

Table 4.3: Rectification statistics

	High	Sample V1			Sample V2			Sample V3		
		Count	rel.	abs. [A]	Count	rel.	abs. [A]	Count	rel.	abs. [A]
A1-B	A1+	62%	208%	4,98E-07	67%	213%	2,74E-07	71%	307%	2,58E-07
	A1-	17%	48%	-3,83E-07	33%	79%	-8,63E-08	29%	61%	-7,39E-08
A2-B	A2+	21%	448%	3,16E-10	20%	178%	5,65E-11	0%		
	A2-	79%	25%	-8,16E-09	80%	19%	-3,84E-10	100%	16%	-2,84E-10
B-C	B+	31%	288%	1,54E-10	50%	202%	2,19E-11	32%	554%	4,10E-11
	B-	58%	45%	-7,21E-08	39%	62%	-1,05E-11	58%	58%	-6,85E-12
C-D	C+	65%	710%	9,55E-10	77%	715%	5,12E-10	67%	688%	1,15E-11
	C-	27%	52%	-8,34E-11	23%	67%	-7,70E-12	33%	64%	-1,06E-08
Total count		> 26			> 26			> 19		
E-F (top)	E+	100%	329%	2,55E-9	60%	279%	1,11E-8	67%	171%	1,27E-9
	E-									
Total count		= 7			= 5			= 6		

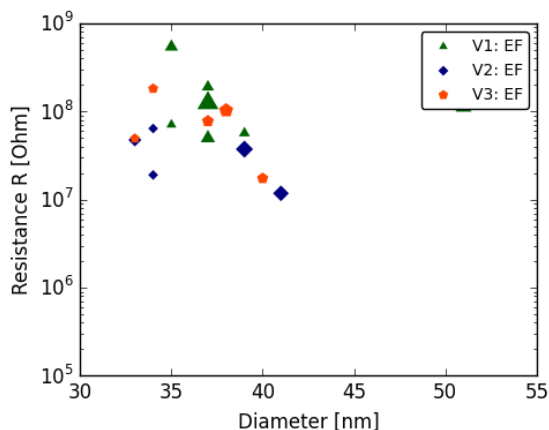


Figure 4.5: Dependence of the resistance on the shell thickness in E-F; the color and shape marks different samples, the size reflects the relative rectification (legend shows size with no rectification).

from $1 \times 10^7 \Omega$ to $1 \times 10^9 \Omega$.

In the following, the present data is discussed in order to find the major influences on the resistance and the rectification. First of all, the shell thickness seems to determine the order of magnitude of the resistance and can be rated as a major influence (figures 4.3b and 4.4). Consequently, the electrical measurements actually show the wires' properties and are not dominated by Schottky barriers. However, the scattering of the data points spans two orders of magnitude for a given shell thickness and a clear relation between the thickness can therefore not be extracted. One reason for the deviations could be the contact distance, but even for a change over 650 nm a significant trend of the resistance with the contact distance is not visible (compare figure 4.4). Thus, entities related to the volume of the segment, like composition and doping density can be ruled out as a main influence. Furthermore the composition difference is the largest between the samples, but no obvious difference in rectification or resistance behaviour is visible between the samples. (The composition of the shell has an influence on the electron mobility [39] and therefore the resistance) On the core-shell part, strain leads to piezoresistive effects, which directly influences the resistance. Especially the splitting in 4.3a is a feature likely to be explained with piezoresistance. But since it appears in every sample with a similar distribution, it must

be a feature indifferent to the amount of strain and is therefore not related to piezoresistance. The piezoelectric field could cause bending of the bands along the wire and lead to charge accumulation or depletion at the ends of the wire, which in turn changes the carrier concentration and ergo the resistance. This would affect the contact pairs A-B and C-D in the opposite way. In fact, the distributions and resistances are very similar (compare figures 4.3a and 4.3b).

The rectification contains information about the directionality of the electrical properties. Hence, the piezoresistivity and the piezoelectric effect will have an impact on the rectification. Table 4.3 provides the data for the following discussion of the rectification. In sample V1, the major part of the nanowires exposes positive rectifications (higher currents for a positive bias on contact X in X-Y) for the contact combinations A1-B, C-D, and E-F and negative rectifications for A2-B and B-C. Except for sample V2 B-C, the behavior in sample V1 translates to sample V2 and V3 without changes. Assuming that the samples V1 and V3 show reversed strain, the latter argument rules out the piezoresistive and piezoelectric effect as a dominating influence on the rectification behavior. Thus, either a composition gradient or the shell thickness needs to be responsible for the rectification. An unintended composition gradient for the growth of $\text{Ga}_x\text{In}_{1-x}\text{As}$ is likely to appear [13], due to the relatively small diffusion length of gallium compared to indium [40]. Unfortunately, the composition along the shell was not measured and makes every further analysis speculative. The shell thickness remains as a major influence on the measurements of the samples V1, V2, and V3. In the following, an explanation model based on the detailed morphology of the wire is developed. For this purpose, the average morphology of the nanowires was thoroughly investigated. Figure 4.6 shows a qualitative scheme of the nanowire with the contact positions. The morphology's details are strongly exaggerated in the scheme in order to illustrate the model. One important feature of the nanowire is the hidden transition from the core-shell part to the top part, which complicates the precise placement of the contact. Contact A thus lies either on the top (A1) or on the core-shell (A2) part. Considering the large cross section in the top part close to the interface, this explains the splitting of the resistance measurements in A-B (see figure 4.3a). In A-B measurements with low resistances, contact A was placed beyond the interface (A1) and otherwise on the shell (A2). How the shell thickness could influence the rectification, the following explanation is suggested: In the case of quantum confinement in a two dimensional layer, the conduction band of

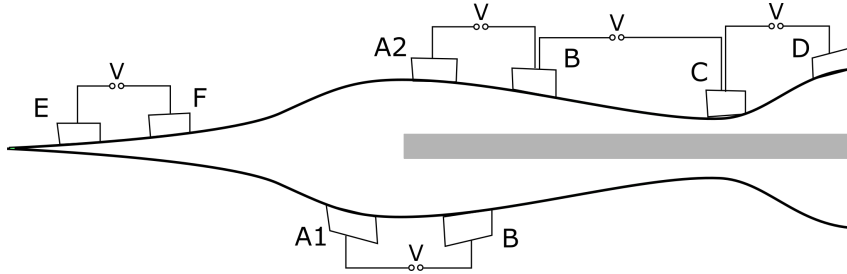


Figure 4.6: Morphology with contact placement of an exemplary sample for V1, V2, or V3.

the material is shifted to higher energies by the term

$$\epsilon_n = \frac{\hbar^2}{2m^*} \frac{\pi}{L^2} n^2 \quad (4.3)$$

with the reduced Planck-constant \hbar , the effective electron mass m^* , thickness L (in the direction of confinement) and the integer $n = 0, 1, 2, \dots$. The energy is inversely proportional to the layer thickness, so that a thinner layer has the bottom of the conduction band at higher energies. A gradient in the layer thickness would then result in a band that is bent down towards thicker layers. This would group the contacts C-D and E-F in one group and A1-B, A2-B, and B-C in the other. Except for the special case A1-B, where the current has to cross the interface to the core-shell part, the grouping fits with the observations above. The model, however, predicts that electrons pass easier from the thinner to the thicker layer. The opposite is the case in the measurements. For the special case A1-B, the model seems to fit perfectly well. In conclusion, the model considers the shell thickness as the main influence of the wires resistance and rectification. The model leads to the same grouping of the contacts observed in the experiments and can explain the low resistance of A1-B and its rectification. The rectification for all the other contacts is strictly the opposite to the expected one and needs another theoretical model to explain it.

4.2.2 SAE InAs-InP core-shell nanowires

Samples grown with SAE do not have a top segment. Consequently, the mean value of the reference core is the only possible approximation to the core ra-

Table 4.4: Rectification statistics

		Sample S3		
	High	Count	rel.	abs. [A]
A-B	A+	86%	587%	1.75E-10
	A-	14%	55%	-8.01E-10
B-C	B+	67%	248%	4.11E-14
	B-	33%	62%	-7,06E-13
C-D	C+	5%	125%	9,86E-14
	C-	95%	55%	-1.42E-13
Total count		A-B: 28, B-C: 9, C-D: 21		

dius and therefore the shell thickness. The reference core has a diameter of 49 nm with a standard deviation of 6 nm (compare table 3.4). This creates an uncertainty in core thickness critical to the results, since the shell thickness was the main influence in the previous section. The factor composition, however, vanishes for the InAs shell. The drawback of a defined composition is the fixed strain, which makes it difficult to distinguish the piezoresistance and the piezoelectric field from other effects. Figure 4.7 and the supporting table 4.4 contain the results for the measurements on sample S3. From both, it can be concluded that A-B has resistances two orders of magnitude lower than C-D and B-C. The dependence on the diameter is not pronounced

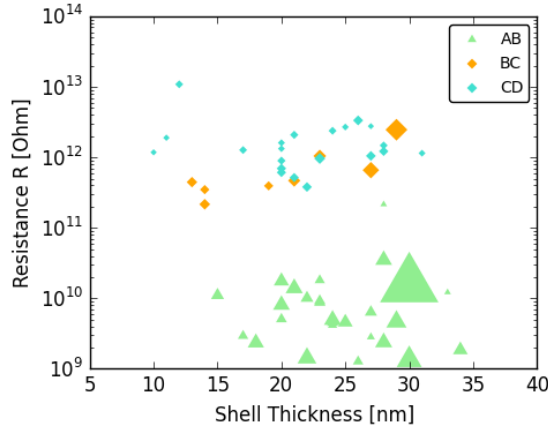


Figure 4.7: Dependence of the resistance on the shell thickness in A-B, B-C, and C-D; the color and shape marks different samples, the size reflects the relative rectification (legend shows size with no rectification).

clearly compared to figures 4.3a and 4.3b. The comparison of the mean resistance and shell thickness in C-D for the samples S3 ($1.93 \times 10^{12} \Omega$, 21 nm), S1 ($5.84 \times 10^3 \Omega$, 58 nm) and V2 ($1.54 \times 10^{10} \Omega$, 9 nm) emphasizes that the layer thickness can not be the only major influence on the resistance. Hence, the model used in the previous section is not sufficient for describing the results in sample S3. The contact quality should mainly depend on the material and the process. Resistances in the order of $k\Omega$ for S1 indicate a good contact quality to the InAs shell. The distances between the contacts A-B and C-D have a standard deviation of less than 19 nm. The distance in B-C deviates by 162 nm. However, a correlation between the deviation of the resistance and the contact distance does not emerge from figure 4.7. Furthermore, the rectification is clearly positive in A-B and clearly negative in C-D. The major part of B-C measurements exhibits positive rectification. Those directional electronic properties are likely to be caused by the directional piezoresistance and piezoelectric field, but since the system has fixed strain, the influence of the strain on the directionality can not be proved.

Possible influences on the electrical properties are the piezoresistance caused by strain in the heterostructure, the piezoelectric field causing charge accumulation or depletion at the ends of the wire, Schottky barriers, dislocations from strain relaxation, and quantum confinement. The information obtained from the measurements and the measurement conception does not allow a separation of those influences.

4.3 Conclusion

This work examined radial nanowire heterostructures with wurtzite InP cores and $\text{Ga}_x\text{In}_{1-x}\text{As}$ shells. A theoretical prediction of the strain and the resulting piezoelectric field using analytical calculations led to an ideal ratio from the shell thickness to the core radius of 0.43 and electrical fields in the order of $1 \times 10^6 \text{ V/m}$. The samples were grown with success using two different growth methods, first, gold seeded growth mode and, secondly, selective area epitaxy. Single nanowires were contacted at 4 positions and a current voltage characterization of the samples provided the resistance and rectifying behavior. For $\text{Ga}_x\text{In}_{1-x}\text{As}$ ($0.3 < x < 0.7$) shells with a thickness smaller than 10 nm, the shell thickness was the main influence on the resistance and the rectification in the sample. The model proposed was based on the nanowires detailed morphology and can explain the resistance of the contacts.

However, the observation that electrons flow more likely towards thinner segments contradicted the model of larger energy barriers, due to the quantum confinement in the shell. For InAs ($x = 0$) shells thicker than 25 nm, the morphology of the nanowire is no longer the dominating influence, but the measurements did not provide enough information to separate the influences. The resistance for thick shells was 60 nm, which indicates good contact quality. If the nanowire heterostructures exhibited strain and piezoelectric fields, the measurements and the samples did not provide the flexibility to isolate the effect from other influences. The aim to prove the piezoelectric field in strained core-shell nanowires was not reached.

Chapter 5

OUTLOOK

The piezoelectric effect could not be shown in the present work. The concept of this project could still lead to success, if the number of uncertainties are reduced: First, the cores' morphology needs to be well known and reproducible. The diameter should be smaller than 40 nm. The most reliable and reproducible results was obtained by SAE growth without subsequent etching procedure. Therefore, a growth mask with small openings would probably lead to reproducible results. Secondly, the composition of the shell must be uniform or known. Thirdly, the shell thickness should be larger than 15 nm to avoid strong influences. Fourthly, the location of the transition needs to be known. If these factors are fulfilled, the measurement approach should be sufficient to extract the piezoelectric effect. Nevertheless, it will require a good theoretical model to estimate the different influences.

In order to avoid that, also the concept of measuring the piezoelectric effect can be revised. One approach could be, to restrict the measurement to the piezoelectric field. A device to achieve this, would be a core-shell heterostructure, where the two ends of the core lie bare and are contacted. Another pair of contacts lies on the shell, close to the edges. The outer pair on the core part could then apply an electric field and the contact pair on the shell part only measures the voltage. If the contacts on the shell show an opposite field to the one applied at any time, the piezoelectric field would be directly visible.

Bibliography

- [1] M. T. Borgström, J. Wallentin, M. Heurlin, S. Fält, P. Wickert, J. Leene, M. H. Magnusson, K. Deppert, and L. Samuelson, “Nanowires with promise for photovoltaics,” *IEEE Journal on Selected Topics in Quantum Electronics*, vol. 17, no. 4, pp. 1050–1061, 2011.
- [2] F. Dimroth and S. Kurtz, “High-efficiency multijunction solar cells,” *Mrs Bulletin*, vol. 32, no. 3, pp. 230–235, 2007.
- [3] J. Wallentin, N. Anttu, D. Asoli, M. Huffman, I. Aberg, M. H. Magnusson, G. Siefert, P. Fuss-Kailuweit, F. Dimroth, B. Witzigmann, H. Q. Xu, L. Samuelson, K. Deppert, and M. T. Borgstrom, “InP Nanowire Array Solar Cells Achieving 13.8% Efficiency by Exceeding the Ray Optics Limit,” *Science*, vol. 339, pp. 1057–1060, mar 2013.
- [4] F. Boxberg, N. Søndergaard, and H. Q. Xu, “Photovoltaics with piezoelectric core-shell nanowires.,” *Nano letters*, vol. 10, no. 4, pp. 1108–12, 2010.
- [5] H. Y. Al-Zahrani, J. Pal, M. a. Migliorato, G. Tse, and D. Yu, “Piezoelectric field enhancement in IIIV coreshell nanowires,” *Nano Energy*, vol. 14, pp. 382–391, 2015.
- [6] X. Feng, Y. Zhang, and Z. Wang, “Theoretical study of piezotronic heterojunction,” *Science China Technological Sciences*, vol. 56, no. 11, pp. 2615–2621, 2013.
- [7] S. C. Rai, K. Wang, Y. Ding, J. K. Marmon, M. Bhatt, Y. Zhang, W. Zhou, and Z. L. Wang, “Piezo-phototronic Effect Enhanced UV/Visible Photodetector Based on Fully Wide Band Gap Type-II ZnO/ZnS Core/Shell Nanowire Array,” *ACS Nano*, vol. 9, no. 6, pp. 6419–6427, 2015.

- [8] P. Liu, H. Huang, X. Liu, M. Bai, D. Zhao, Z. Tang, X. Huang, J. Y. Kim, and J. Guo, “Core-shell nanowire diode based on strain-engineered bandgap,” *Physica Status Solidi (A) Applications and Materials Science*, vol. 212, no. 3, pp. 617–622, 2015.
- [9] F. Glas, J.-C. Harmand, and G. Patriarche, “Why Does Wurtzite Form in Nanowires of III-V Zinc Blende Semiconductors?,” *Physical Review Letters*, vol. 99, no. 14, p. 146101, 2007.
- [10] H. J. Joyce, J. Wong-Leung, Q. Gao, H. H. Tan, and C. Jagadish, “Phase Perfection in Zinc Blende and Wurtzite III-V Nanowires Using Basic Growth Parameters,” *Nano Letters*, vol. 10, no. 3, pp. 908–915, 2010.
- [11] P. Caroff, J. Bolinsson, and J. Johansson, “Crystal phases in III-V nanowires: From random toward engineered polytypism,” *IEEE Journal on Selected Topics in Quantum Electronics*, vol. 17, no. 4, pp. 829–846, 2011.
- [12] Q. Gao, D. Saxena, F. Wang, L. Fu, S. Mokkaapati, Y. Guo, L. Li, J. Wong-Leung, P. Caroff, H. H. Tan, and C. Jagadish, “Selective-Area Epitaxy of Pure Wurtzite InP Nanowires: High Quantum Efficiency and Room-Temperature Lasing,” *Nano letters*, vol. 14, pp. 5206–5211, 2014.
- [13] A. S. Ameruddin, H. A. Fonseka, P. Caroff, J. Wong-Leung, R. L. Ophthel Veld, J. L. Boland, M. B. Johnston, H. H. Tan, and C. Jagadish, “In_{1-x}Ga_xAs nanowires with uniform composition, pure wurtzite crystal phase and taper-free morphology,” *Nanotechnology*, vol. 26, no. 20, p. 205604, 2015.
- [14] D. Ferrand and J. Cibert, “Strain in crystalline core-shell nanowires,” *The European Physical Journal Applied Physics*, vol. 67, no. 3, p. 30403, 2014.
- [15] H.-L. Cui, W. Zhang, Y. Cheng, and X.-R. Chen, “Structural and Thermodynamic Properties of Gallium Arsenide with Hexagonal Wurtzite Structure from First-Principles Analysis,” *Chinese Physics Letters*, vol. 24, pp. 814–817, 2007.
- [16] M. Levinshtein, S. Rumyantsev, and M. Shur, *Handbook Series on Semiconductor Parameters*, vol. 1. WORLD SCIENTIFIC, nov 1996.

- [17] D. Kriegner, C. Panse, B. Mandl, K. a. Dick, M. Keplinger, J. M. Persson, P. Caroff, D. Ercolani, L. Sorba, F. Bechstedt, J. Stangl, and G. Bauer, “Unit cell structure of crystal polytypes in InAs and InSb nanowires,” *Nano Letters*, vol. 11, no. 4, pp. 1483–1489, 2011.
- [18] D. Kriegner, E. Wintersberger, K. Kawaguchi, J. Wallentin, M. T. Borgström, and J. Stangl, “Unit cell parameters of wurtzite InP nanowires determined by x-ray diffraction,” *Nanotechnology*, vol. 22, no. 42, p. 425704, 2011.
- [19] S. Q. Wang and H. Q. Ye, “First-principles study on elastic properties and phase stability of III–V compounds,” *phys. stat. sol. (b)*, vol. 240, no. 1, pp. 45–54, 2003.
- [20] C. Hajlaoui, L. Pedesseau, F. Raouafi, F. Ben Cheikh Larbi, J. Even, and J.-M. Jancu, “Ab initio calculations of polarization, piezoelectric constants, and elastic constants of InAs and InP in the wurtzite phase,” *Journal of Experimental and Theoretical Physics*, vol. 121, no. 2, pp. 246–249, 2015.
- [21] V. Chin, “Reassessment of the piezoelectric constant in GaAs by studying the electron transport of high purity MBE-grown GaAs,” *Solid-State Electronics*, vol. 37, no. 7, pp. 1345–1347, 1994.
- [22] F. Boxberg, N. SaØndergaard, and H. Q. Xu, “Elastic and piezoelectric properties of zincblende and wurtzite crystalline nanowire heterostructures,” *Advanced Materials*, vol. 24, no. 34, pp. 4692–4706, 2012.
- [23] O. Salehzadeh, K. L. Kavanagh, and S. P. Watkins, “Geometric limits of coherent III-V core/shell nanowires,” *Journal of Applied Physics*, vol. 114, no. 5, p. 054301, 2013.
- [24] A. Fontcuberta i Morral, S. A. Dayeh, and C. Jagadish, *Semiconductor Nanowires I: Growth and Theory, 1st Edition*. Waltham: Academic Press, 1 ed., 2015.
- [25] E. J. Thrush, C. G. Cureton, and J. M. Trigg, “Reactor design and operating procedures for InP-based MOCVD,” *Chemtronics*, vol. 2, no. 2, pp. 62–68, 1987.

- [26] G. B. Stringfellow, *Organometallic vapor-phase epitaxy: theory and practice*. 2 ed., 1998.
- [27] S. Bhunia, T. Kawamura, S. Fujikawa, H. Nakashima, K. Furukawa, K. Torimitsu, and Y. Watanabe, “Vaporliquid-solid growth of vertically aligned InP nanowires by metalorganic vapor phase epitaxy,” *Thin Solid Films*, vol. 464-465, pp. 244–247, 2004.
- [28] S. Paiman, Q. Gao, H. J. Joyce, Y. Kim, H. H. Tan, C. Jagadish, X. Zhang, Y. Guo, and J. Zou, “Growth temperature and V/III ratio effects on the morphology and crystal structure of InP nanowires,” *Journal of Physics D: Applied Physics*, vol. 43, no. 44, p. 445402, 2010.
- [29] H. J. Joyce, J. Wong-Leung, C. K. Yong, C. J. Docherty, S. Paiman, Q. Gao, H. H. Tan, C. Jagadish, J. Lloyd-Hughes, L. M. Herz, and M. B. Johnston, “Ultralow surface recombination velocity in InP nanowires probed by terahertz spectroscopy,” *Nano Letters*, vol. 12, no. 10, pp. 5325–5330, 2012.
- [30] P. Mohan, J. Motohisa, and T. Fukui, “Controlled growth of highly uniform, axial/radial direction-defined, individually addressable InP nanowire arrays,” *Nanotechnology*, vol. 16, no. 12, pp. 2903–2907, 2005.
- [31] M. Heurlin, T. Stankevič, S. Mickevičius, S. Yngman, D. Lindgren, A. Mikkelsen, R. Feidenhansl, M. T. Borgström, and L. Samuelson, “Structural Properties of Wurtzite InPInGaAs Nanowire CoreShell Heterostructures,” *Nano Letters*, vol. 15, no. 4, pp. 2462–2467, 2015.
- [32] M. T. Borgström, J. Wallentin, J. Trägårdh, P. Ramvall, M. Ek, L. R. Wallenberg, L. Samuelson, and K. Deppert, “In situ etching for total control over axial and radial nanowire growth,” *Nano Research*, pp. 1–7, 2010.
- [33] R. E. Algra, M. a. Verheijen, M. T. Borgström, L.-F. Feiner, G. Immink, W. J. P. van Enkevort, E. Vlieg, and E. P. a. M. Bakkers, “Twinning superlattices in indium phosphide nanowires,” *Nature*, vol. 456, no. 7220, pp. 369–372, 2008.
- [34] K. W. Schwarz, J. Tersoff, S. Kodambaka, and F. M. Ross, “Jumping-catalyst dynamics in nanowire growth,” *Physical Review Letters*, vol. 113, no. 5, pp. 1–5, 2014.

- [35] F. Glas, “Chemical potentials for Au-assisted vapor-liquid-solid growth of III-V nanowires,” *Journal of Applied Physics*, vol. 108, no. 7, pp. 1–7, 2010.
- [36] D. B. Suyatin, C. Thelander, M. T. Björk, I. Maximov, L. Samuelson, M. T. Björk, I. Maximov, and L. Samuelson, “Sulfur passivation for ohmic contact formation to InAs nanowires,” *Nanotechnology*, vol. 18, no. 10, p. 105307, 2007.
- [37] P. Holoborodko, “Smooth noise-robust differentiators.”
- [38] S. Crawford, S. K. Lim, and S. Gradečak, “Fundamental Insights into Nanowire Diameter Modulation and the Liquid/Solid Interface,” *Nano Letters*, vol. 13, pp. 226–232, jan 2013.
- [39] D. Chattopadhyay, S. K. Sutradhar, and B. R. Nag, “Electron transport in direct-gap III-V ternary alloys,” *Journal of Physics C: Solid State Physics*, vol. 14, no. 6, 1981.
- [40] J. Wu, B. M. Borg, D. Jacobsson, K. a. Dick, and L.-E. Wernersson, “Control of composition and morphology in InGaAs nanowires grown by metalorganic vapor phase epitaxy,” *Journal of Crystal Growth*, vol. 383, pp. 158–165, 2013.
- [41] J. Gronqvist, N. Sondergaard, F. Boxberg, T. Guhr, S. Aberg, and H. Q. Xu, “Strain in semiconductor core-shell nanowires,” *Journal of Applied Physics*, vol. 106, no. 5, p. 053508, 2009.

Appendix A

STRAIN CALCULUS

The strain distribution in real core-shell nanowires will depend on a large diversity of factors, varying from each individual nanowire. As usual, the attempt to precisely model the reality will not lead to an end. Therefore simpler models are required, which can describe the system reasonably well. Initially it is assumed, that the lattice mismatch f , defined by the two lattice constants a_c and a_s of the unstrained core and shell (see equation A.1), is fully accommodated. No relaxation will be taken into account.

$$f = \frac{(a_s - a_c)}{a_c} \quad (\text{A.1})$$

This alignment at the interface shifts the atoms from their equilibrium position \vec{r} to a new one. Those two positions are related by the displacement field $\mathbf{u}(\vec{r})$. The symmetric part of the fields derivatives then accurately describe the strain ϵ (equation A.2).

$$\epsilon_{ij} = \frac{1}{2} \left(\frac{\partial u_i}{\partial x_j} + \frac{\partial u_j}{\partial x_i} \right) \quad (\text{A.2})$$

A displacement of atoms from their equilibrium position then requires a new balance of forces. In this case the stress and the body forces per unit volume $\mathbf{F}(\vec{r})$ build this new equilibrium (equation A.3).

A set of equations fully describing the elastic strain in any heterostructure will be obtained if the stress σ_{ij} of the equilibrium condition is related to strain. For the case of elastic strain, a stiffness tensor can connect those two entities in the manner of Hook (see A.4). The obtained expression is called

Lamé-Clapeyron-Navier equation (A.5). One for each i and $x_i = x, y, z$ will then form a complete set to describe the strain in the crystal.

$$\sum_j \frac{\partial \sigma_{ij}}{\partial x_j} + F_i = 0 \quad (\text{A.3})$$

$$\sigma_{ij} = \sum_{kl} c_{ijkl} \epsilon_{kl} \quad (\text{A.4})$$

$$\sum_{jkl} c_{ijkl} \frac{\partial}{\partial x_j} \left(\frac{\partial u_k}{\partial x_l} + \frac{\partial u_l}{\partial x_k} \right) + F_i = 0 \quad (\text{A.5})$$

The number of terms in equation A.5 can be reduced drastically by boundary conditions and symmetry, which is the aim of the next steps. Before that, it should be noted, that a cylindrical coordinate system was used. The elements of the displacement field are then u_r , u_θ , and u_z , which are defined by $u_x = u_r(r) \cos \theta$ and $u_y = u_r(r) \sin \theta$. The main axis z is chosen to be parallel to interface and surface and lies in the center of the heterostructure. Such a coordinate system is convenient for cylindrical heterostructures and simplifies the calculation for the case of cylindrical symmetry, which will be important later in the chapter.

Two boundary conditions stabilize the surface and the interface. First, the stress on both sides of the interface needs to be equal, meaning $\sigma_{rr}^c = \sigma_{rr}^s$, where the indices c and s mark the core and the shell. Secondly, Surface stress is not allowed ($\sigma_{rr}^s(r_s) = 0$). Additionally it must be implemented, that the displacement field fully compensates for the lattice mismatch.

The effect of symmetry on the equation system needs to be evaluated for both crystal structures separately. In the case of wurtzite, the direction [0001] has cylindrical symmetry and the polarization is large, when it is strained. Therefore the calculations will restrict to heterostructures with the z -axis aligned to [0001]. From cylindrical symmetry follows, that the elements $\sigma_{r\theta}$ and σ_{rz} automatically vanish and σ_{zz}^c and σ_{zz}^s are uniform. The latter results in the condition $\eta \sigma_{zz}^c + (1 - \eta) \sigma_{zz}^s = 0$. Symmetry has a particularly large effect on the stiffness tensor with 36 independent elements. Equation A.6 provides the stiffness tensor in Voigt notation for wurtzite crystals oriented

in [0001].

$$\left(\begin{array}{cccccc} c_{11} & c_{12} & c_{13} & 0 & 0 & 0 \\ c_{12} & c_{11} & c_{13} & 0 & 0 & 0 \\ c_{13} & c_{13} & c_{33} & 0 & 0 & 0 \\ 0 & 0 & 0 & c_{44} & 0 & 0 \\ 0 & 0 & 0 & 0 & c_{44} & 0 \\ 0 & 0 & 0 & 0 & 0 & \frac{c_{11}-c_{12}}{2} \end{array} \right) \quad (\text{A.6})$$

The result has only five independent elements and is invariant to rotation around the z-axis. Furthermore, the wire is assumed to be infinitely long, which leads to translational invariance of all $\mathbf{u}(\vec{r})$ derivatives. According to Saint Venant's principle this simplification does not influence any segment separated from the ends of the wire by the length of the wire diameter. Thorough simplification of the Lamé-Clapeyron-Navier equations [14] with the stated boundary conditions and symmetry arguments, lead to the following results:

$$\begin{aligned} \epsilon_{zz}^c &= \frac{(1-\eta)\chi}{\eta + (1-\eta)\chi} f_{\parallel} \\ \epsilon_{zz}^s &= \frac{-\eta}{\eta + (1-\eta)\chi} f_{\parallel} \\ \frac{\epsilon_{\theta\theta}^c - \epsilon_{rr}^c}{2} &= 0 \\ \frac{\epsilon_{\theta\theta}^s - \epsilon_{rr}^s}{2} &= B_s \frac{r_c^2}{r^2} \\ \frac{\epsilon_{\theta\theta}^c + \epsilon_{rr}^c}{2} &= \frac{(1-\eta)\chi}{\eta + (1-\eta)\chi} (f_{\perp} + B_s) \\ \frac{\epsilon_{\theta\theta}^s + \epsilon_{rr}^s}{2} &= \frac{-\eta}{\eta + (1-\eta)\chi} (f_{\perp} + B_s) \end{aligned} \quad (\text{A.7})$$

with

$$\begin{aligned} B_s &= -\frac{(c_{11} + c_{12})f_{\perp} + c_{13}f_{\parallel}}{(c_{11} - c_{12})[\eta + (1-\eta)\chi] + (c_{11} + c_{12})} \\ (f_{\perp} + B_s) &= \frac{(c_{11} - c_{12})[\eta + (1-\eta)\chi]f_{\perp} - c_{13}f_{\parallel}}{(c_{11} - c_{12})[\eta + (1-\eta)\chi] + (c_{11} + c_{12})} \end{aligned} \quad (\text{A.8})$$

The area ratio of the circular cross sections is $\eta = r_c^2/r_s^2$ and the Poisson ratio χ is averaged over each term $\chi = c_{ijkl}^s/c_{ijkl}^c$, which is a good approximation

in the present case. Two different mismatches are needed in the hexagonal structure: f_{\perp} is perpendicular and f_{\parallel} is parallel to the interface.

In cubic zincblende crystals, the (111) plane is isotropic to some mechanical properties, so the cylindrical approximation is therefore a natural choice [14]. The coordinate system is then $x = [1\bar{1}0]$, $y = [11\bar{2}]$, and $z = [111]$. The stiffness matrix with six (dependent) components is then

$$\left\{ \begin{array}{cccccc} \tilde{c}_{11} & \tilde{c}_{12} & \tilde{c}_{13} & \tilde{c}_{14} & 0 & 0 \\ \tilde{c}_{12} & \tilde{c}_{11} & \tilde{c}_{13} & -\tilde{c}_{14} & 0 & 0 \\ \tilde{c}_{13} & \tilde{c}_{13} & \tilde{c}_{33} & 0 & 0 & 0 \\ \tilde{c}_{14} & -\tilde{c}_{14} & 0 & \tilde{c}_{44} & 0 & 0 \\ 0 & 0 & 0 & 0 & \tilde{c}_{44} & \tilde{c}_{14} \\ 0 & 0 & 0 & 0 & \tilde{c}_{14} & \frac{\tilde{c}_{11}-\tilde{c}_{12}}{2} \end{array} \right\} \quad (\text{A.9})$$

with

$$\begin{aligned} \tilde{c}_{13} &= \frac{1}{2}c_{11} + \frac{1}{2}c_{12} + c_{44} \\ \tilde{c}_{13} &= \frac{1}{3}c_{11} + \frac{2}{3}c_{12} + \frac{4}{3}c_{44} \\ \tilde{c}_{13} &= \frac{1}{6}c_{11} + \frac{5}{6}c_{12} - \frac{2}{6}c_{44} \\ \tilde{c}_{13} &= \frac{1}{3}c_{11} + \frac{2}{3}c_{12} - \frac{2}{3}c_{44} \\ \tilde{c}_{13} &= \frac{1}{3}c_{11} - \frac{1}{3}c_{12} + \frac{1}{3}c_{44} \\ \tilde{c}_{13} &= \frac{1}{3\sqrt{2}}(c_{11} - c_{12} - 2c_{44}) \end{aligned} \quad (\text{A.10})$$

Using the same boundary conditions as above, translational invariance along z , and the symmetry of the crystal structure, the Lamé-Clapeyron-Navier equations can be simplified to a set of equations equivalent to A.7 (review [14] for more details). The lattice mismatch, however, reduces to $f_{\parallel} = f_{\perp} = f$ and the parameters of A.8 are changed to

$$\begin{aligned} B_s &= -\frac{3(c_{11} + 2c_{12})}{(c_{11} - c_{12} + 4c_{44})[\eta + (1 - \eta)\chi] + (2c_{11} + 4c_{12} + 2c_{44})} \\ (f_{\perp} + B_s) &= -\frac{(c_{11} - c_{12} + 4c_{44})[\eta + (1 - \eta)\chi] - (c_{11} + 2c_{12} - 2c_{44})}{(c_{11} - c_{12} + 4c_{44})[\eta + (1 - \eta)\chi] + (2c_{11} + 4c_{12} + 2c_{44})} \end{aligned} \quad (\text{A.11})$$

With equations A.7, A.8, and A.11 analytical calculation of strain in core shell nanowires is possible for cylindrical nanowires. For the case of radial wurtzite heterostructures grown along [0001] the result is correct [14]. In the case of zincblende grown along [111], the shell is warped [41] Nevertheless, the analytical result is very close to more advanced three dimensional calculations (see the work of Ferrand et al. for more details) and therefore a good approximation.

The relevant strain components for piezoelectric polarization in the two systems described above are ϵ_{zz} and $(\epsilon_{rr} + \epsilon_{\theta\theta})$ (for wurtzite) or $(2\epsilon_{zz} - \epsilon_{yy} - \epsilon_{xx})$ (for zincblende) [4]. The piezoelectric polarization in z-direction is then given by

$$\begin{aligned} P_z^{wz} &= e_{31}(\epsilon_{rr} + \epsilon_{\theta\theta}) + e_{33}\epsilon_{zz} \\ P_z^{zb} &= \frac{e_{14}}{\sqrt{3}}(2\epsilon_{zz} - \epsilon_{yy} - \epsilon_{xx}) \end{aligned} \quad (\text{A.12})$$

while wurtzite crystals have two piezoelectric constants, e_{31} and e_{33} , and zincblende crystals one, e_{14} . The polarization adds up along the crystal and turns nanowires of finite lengths into dipoles. A first approximation of the field is the average effective surface charge density $\langle \rho_s^{pz} \rangle$ divided by the average electrical permittivity $\langle \epsilon \rangle$ [4]:

$$E_z = \frac{\langle \rho_s^{pz} \rangle}{\langle \epsilon \rangle} = -\frac{P_{z,c}A_c + P_{z,s}A_s}{\epsilon_0(\epsilon_c A_c + \epsilon_s A_s)} \quad (\text{A.13})$$

while A_c and A_s denote the cross section areas of core and shell, ϵ_c and ϵ_s are the permittivity of the core and the shell, and ϵ_0 is the vacuum permittivity.

In summary, the formulas provided here allow an analytical calculation of strain and an assessment of the piezoelectric polarization along [0001] in wurtzite structures and [111] in zincblende structures.